CK2 signaling from TOLLIP-dependent perinuclear endosomes is an essential feature of *KRAS* and *NRAS* mutant cancers

Srikanta Basu[1], Brian T. Luke[2], Baktiar Karim[3], Nancy Martin[1], Stephen Lockett[4], Sudipto Das[5], Thorkell Andresson[5], Karen Saylor[3], Serguei Kozlov[6], Laura Bassel[6], Dominic Esposito[7], Mélissa Galloux[8], and Peter F. Johnson[1*]

[1]Mouse Cancer Genetics Program, Center for Cancer Research, National Cancer Institute, Frederick, Maryland, USA; [2]Advanced Biomedical Computational Science, Frederick National Laboratory for Cancer Research, Frederick, MD, USA; [3]Laboratory Animal Sciences Program, Frederick National Laboratory for Cancer Research, Frederick, MD, USA; [4]Optical Microscopy and Image Analysis Laboratory, Cancer Research Technology Program, Frederick National Laboratory for Cancer Research, Frederick, Maryland, USA; [5]Protein Characterization Laboratory, Cancer Research Technology Program, Leidos Biomedical Research, Inc., Frederick National Laboratory for Cancer Research, Frederick, Maryland, USA; [6]Center for Advanced Preclinical Research, Frederick National Laboratory for Cancer Research, NCI, Frederick, Maryland, USA; [7]NCI RAS Initiative, Frederick National Laboratory for Cancer Research, Leidos Biomedical Research, Inc., Frederick, Maryland, USA; [8]Independent Bioinformatician, Marseille, France

***Corresponding author**

Abstract

Oncogenic RAS induces perinuclear translocation of the effector kinases ERK and CK2 and their scaffold, KSR1, forming endosomal signaling hubs termed perinuclear signaling centers (PSCs). PSCs are present in all cancer cell lines and tissues examined, suggesting that subcellular compartmentalization of oncogenic kinases drives tumorigenesis. However, the mechanism of perinuclear targeting, whether this location affects kinase substrate specificity, and the importance of PSCs in cancer are unclear. Here we show that the endosomal adaptor, TOLLIP, specifically tethers RAB11A^{+} signaling endosomes containing CK2 and KSR1 to the perinuclear ER. A predicted β-hairpin fold in TOLLIP mediates binding to the KSR1 CA5 pseudo-kinase domain, recruiting CK2/KSR1 complexes to perinuclear endosomes. TOLLIP is essential for proliferation/survival of tumor cells carrying *KRAS* and *NRAS* mutations but not *HRAS*, *BRAF*, *ERBB* or *PTEN* lesions, or non-transformed cells. *KRas*^{G12D}-induced lung lesions in *Tollip*$^{-/-}$ mice displayed reduced numbers of carcinomatous lesions, implicating TOLLIP in malignant progression. TOLLIP-dependent perinuclear CK2 was shown to phosphorylate discrete substrates, including proteins involved in translation and ribosome biogenesis such as RIOK1. Thus, TOLLIP is a key RAS pathway signaling adaptor in *K/NRAS* tumors whose inhibition is a specific vulnerability of these cancers.

50 *RAS* proto-oncogenes are among the most frequently mutated in cancer, with ~19% of patients
51 harboring *RAS* alterations[1]. *RAS* cancers are particularly aggressive and treatment-refractory[2,3].
52 *KRAS* is the most prevalent mutant RAS isoform, representing 75% of all *RAS* cancers. *KRAS*
53 mutations are observed in 88%, 50% and 32% of pancreatic, colon and lung cancer patients,
54 respectively, while *NRAS* alterations are predominant in melanoma and *HRAS* in thyroid and
55 endometrial cancers[1,4]. Oncogenic RAS typically triggers elevated, constitutive signaling through
56 the RAF-MEK-ERK kinase cascade. Studies using integrative pharmacogenomics and
57 phosphoproteomics have also demonstrated an essential role for CK2 kinase in KRAS-driven lung
58 and pancreatic adenocarcinomas (ADCs)[5,6,7]. Despite the importance of RAS effector kinases in
59 tumorigenesis, drugs targeting these kinases have not produced durable therapeutic responses[8,9].
60 Therefore, it is important to explore additional features of oncogenic RAS signaling that may
61 uncover novel drug targets.

62 A comprehensive molecular characterization of human lung ADCs showed that p-ERK levels
63 are moderate or low in a substantial proportion of tumor samples, including many that harbor
64 *KRAS* mutations[10]. Similar findings were described for certain lung, colorectal, and pancreatic
65 cancer cell lines[11,12,13,14] and endometrial tumor samples[15], suggesting that characteristics besides
66 high MAPK pathway output can contribute to RAS tumorigenesis. Receptors, kinases, scaffolds
67 and RAS proteins can be internalized and signal from endo-membranes[16]. However, the functional
68 consequences of this subcellular compartmentalization, such as whether it influences the substrate
69 selectivity of effector kinases, are unclear. There is also scant information on whether
70 compartmentalized signaling differs in transformed and normal cells. In this regard, we previously
71 reported that RAS-induced transformation coincides with perinuclear re-localization of p-ERK1/2,
72 CK2 and the MAPK scaffold KSR1, which binds to both kinases[17]. These proteins form signaling

73 hubs on nuclear-proximal endosomes termed perinuclear signaling centers (PSCs) that require
74 KSR1 and endosomal trafficking. CK2 and KSR1, but not p-ERK, colocalize with the recycling
75 endosome (RE) marker, RAB11A[17]. In serum-stimulated normal cells, CK2 and p-ERK undergo
76 delayed, transient perinuclear localization, albeit with different kinetics (4 and 6 h post-
77 stimulation, respectively). These findings demonstrate that ERK1/2 and CK2 are associated with
78 distinct types of endosomes.

79 PSCs are present in all cancer cell lines tested and *KRas*^{G12D}-driven mouse lung tumors but
80 not in non-transformed cells or normal lung tissue[17]. These observations suggest that PSC kinases
81 are involved in transducing signals from active RAS, functioning as critical signaling platforms in
82 tumor cells. Therefore, we sought to elucidate the mechanisms that control perinuclear segregation
83 of PSCs, test their functional importance in tumor cells and determine whether PSC-associated
84 kinases selectively phosphorylate specific substrates. We report that the endosomal adaptor and
85 ubiquitin binding protein, TOLLIP, tethers endosomes containing CK2 but not ERK to the
86 perinuclear ER, and that *KRAS* and *NRAS* mutant tumor cells are specifically dependent on
87 TOLLIP for proliferation/survival. We also identify a phosphoproteome requiring perinuclear
88 CK2, demonstrating the importance of subcellular localization in oncogenic signaling.

89

90 Results

91 TOLLIP co-localizes with RAB11A^{+} CK2 signaling endosomes in tumor cells

92 Endocytosis regulates the intracellular sorting, distribution, degradation and recycling of cargo
93 proteins, and modification of endosome trafficking in cancer cells is known to promote
94 tumorigenesis[18,19]. It has been shown that endosomes exist in two spatially distinct but dynamic
95 pools: fast moving peripheral endosomes (PPE) and slow moving perinuclear endosomes (PNE)[20].

96 PNEs are tethered to the ER through association with the endosomal adaptor proteins EPS15,
97 TOLLIP or TAX1BP1, which bind to mono-ubiquitinated SQSTM1 (p62) on ER membranes.
98 Therefore, we hypothesized that one or more of these adaptors could be involved in perinuclear
99 targeting of signaling endosomes in tumor cells (Supplementary Fig. 1a).

100 Since KSR1 interacts with multiple RAS effector proteins[21,22,23] and is required for PSC
101 formation[17], we asked whether KSR1 binds to endosomal adaptors. Immunoprecipitation
102 experiments in transfected HEK293T cells showed that Pyo-tagged KSR1 associated with
103 endogenous TOLLIP and *vice versa* (Fig. 1a and Supplementary Fig. 1b). This interaction was not
104 stimulated by oncogenic KRAS. Data mining from several published RNAi screens in tumor cell
105 lines revealed TOLLIP as a dependency gene in three studies, two of which involved *KRAS* mutant
106 cells[24,25,26]. These observations prompted us to further investigate the role of TOLLIP in oncogenic
107 signaling.

108 Live imaging of EGFP-TOLLIP in A549 cells (human $KRAS^{G12S}$ lung ADC) showed that
109 TOLLIP localized exclusively to perinuclear puncta, whereas it displayed diffuse, granular pan-
110 cytoplasmic distribution and a perinuclear component in non-transformed HBEC human bronchial
111 epithelial cells (Fig. 1b; Supplementary Videos 1, 2). Nuclear proximity was quantified using an
112 algorithm that measures the distance of cytoplasmic signals from the nuclear envelope, normalized
113 to a uniformly generated distribution for each cell (relative nuclear proximity index, or RNPI). The
114 mean $RNPI^{TOLLIP}$ in A549 cells was 0.4222 and 0.6831 in HBEC cells, indicating a more
115 perinuclear pattern in tumor cells ($p<0.0001$; Student's t test). These distinct spatial patterns were
116 also seen for fluorescently-tagged KSR1 and CK2α in the two cell lines (Supplementary Fig. 1c;
117 Supplementary Videos 3, 4), and for endogenous TOLLIP, KSR1 and CK2α (Supplementary Fig.
118 1d). p-ERK was also perinuclear in A549 cells but its levels were low in HBEC cells, as expected.

119 Furthermore, CK2α, p-ERK and TOLLIP formed juxtanuclear puncta in the pancreatic ductal
120 adenocarcinoma (PDAC) cell line, PANC1 (*KRAS*^{G12D}) (Supplementary Fig. 1e).

121 TOLLIP partially overlapped with KSR1 in A549 cells and displayed prominent co-
122 occurrence with CK2α (Fig. 1c), which was especially evident in live cell imaging (Fig. 1d).
123 However, TOLLIP had minimal overlap with p-ERK. CK2α resides on RAB11A^{+} slow recycling
124 endosomes in tumor cells[17]. Accordingly, IF (Fig. 1c) and live imaging (Fig. 1d) revealed abundant
125 co-localization of TOLLIP with RAB11A, and RAB11A with CK2α and KSR1 (Supplementary
126 Fig. 1f). These conclusions were supported by quantification of signal colocalization using
127 Pearson's correlation and Manders overlap coefficients. Proximity ligation assays further
128 confirmed the overlap of TOLLIP with CK2α, KSR1 and RAB11A but not p-ERK (Fig. 1e). Taken
129 together, these data show that CK2, TOLLIP, and a fraction of KSR1 localize to perinuclear
130 RAB11A+ endosomes in tumor cells, while ERK resides on a distinct endosomal population.

131 To test our prediction that PSCs occur on ER-tethered endosomes, we analyzed A549 cells
132 co-expressing TOLLIP-mCherry and the ER marker, EGFP-Sec61β. TOLLIP-positive endosomes
133 were wholly embedded within the perinuclear ER network (Fig. 1f; Supplementary Video 5).
134 Endosomes expressing fluorescently-tagged CK2α, KSR1 and RAB11A were also restricted to
135 this domain. Thus, perinuclear compartmentalization of signaling endosomes involves their
136 intimate association with the ER, which demarcates the PSC region.

137 We previously observed juxtanuclear localization of KSR1, CK2 and p-ERK in *KRas*^{G12D}-
138 driven mouse lung adenomas and ADCs but not in adjacent normal tissue[17]. Similarly, Tollip
139 displayed intense perinuclear staining in lung ADCs but was pan-cytoplasmic in normal lung
140 epithelium (Supplementary Fig. 1g). Tollip was also perinuclear in PDACs arising in *LSL-*
141 *Kras*^{G12D}*/+;p53*^{R172H}*/+;Pdx-Cre tg/+* (*KPC*) mice (Supplementary Fig. 1h) and in orthotopic

142 xenografts from a *KPC* PDAC-derived cell line but was diffusely cytoplasmic in normal pancreas
143 (Supplementary Fig. 1i). Thus, the differential subcellular partitioning of TOLLIP seen in tumor
144 vs. non-transformed cell lines extends to *in vivo* tumor tissue.
145

146 **TOLLIP is essential for perinuclear targeting of CK2 and tumor cell proliferation**

147 We next asked whether TOLLIP is required for PSC formation in tumor cells. TOLLIP silencing
148 by two different shRNAs in A549 cells disrupted perinuclear localization of KSR1, CK2α and
149 RAB11A, leading to pan-cytoplasmic distribution of each protein (Fig. 2a). However, p-ERK was
150 not significantly affected (Supplementary Fig. 2a). Similar results were seen in PANC1 cells
151 (Supplementary Fig. 2b). TOLLIP silencing also severely reduced the rate of increase in A549 and
152 PANC1 cell populations (Fig. 2b) and another *KRAS* mutant PDAC cell line, MIA PaCa-2
153 (Supplementary Fig. 2c). The growth defect in A549 cells was associated with increased
154 senescence and apoptosis (Fig. 2c). By contrast, TOLLIP deficiency had little effect on non-
155 transformed HBEC cells (Fig. 2d) or MEFs, as *Tollip*$^{-/-}$ cells grew similarly to *WT* controls
156 (Supplementary Fig. 2d).

157 As TOLLIP, KSR1 and CK2α are associated with RAB11A^{+} endosomes, we investigated
158 whether RAB11A is required for their perinuclear localization. All three proteins became pan-
159 cytoplasmic upon RAB11A silencing (Fig. 2e,f). RAB11A depletion also impaired A549 cell
160 proliferation (Supplementary Fig. 2e). Conversely, TOLLIP was unaffected by KSR1 depletion,
161 although CK2 became dispersed (Supplementary Fig. 2f)[17]. These data suggest that TOLLIP
162 dependency in tumor cells involves its ability, at least in part, to localize CK2 signaling endosomes
163 to the ER. The results support a model in which KSR1 links CK2 to perinuclear RAB11A^{+}

164 endosomes by binding to TOLLIP, which also tethers these vesicles to the ER independently of
165 KSR1.
166
167 **A highly conserved sequence in TOLLIP interacts with the KSR1 CA5 domain**
168 Since KSR1-TOLLIP association appears to recruit signaling complexes to perinuclear
169 endosomes, we sought to further characterize this interaction. We generated a nested set of Pyo-
170 tagged KSR1 C-terminal deletion mutants with endpoints at the N-terminal boundaries of five
171 conserved areas (CA1-5) corresponding to known functional domains (Supplementary Fig. 3a)[27].
172 CA1 binds BRAF and contributes to KSR1 membrane association, CA3 has similarity to atypical
173 C1 lipid binding domains[28] and binds CK2[23], CA4 binds ERK[29], and CA5 is a pseudokinase
174 domain homologous to RAF kinases that interacts with MEK[21,22,30] and RAF[31]. Co-IP experiments
175 using Pyo-KSR1 deletion mutants expressed with rat HA-Tollip in HEK293T cells showed that
176 removal of CA5 (denoted CA1-4) abolished the KSR1-Tollip interaction (Supplementary Fig. 3a).
177 Interestingly, further deletion of CA4 (CA1-3) partially restored Tollip binding, while loss of CA3
178 (CA1-2) eliminated the interaction altogether. The CA5 domain alone also bound Tollip
179 efficiently. Thus, KSR1 CA5 appears to be the major site of Tollip interaction. CA3 is also capable
180 of binding Tollip but this association is inhibited by CA4.
181 To map the corresponding interaction site on Tollip, we performed co-IP assays using Pyo-
182 KSR1 and HA-tagged WT Tollip or various deletion mutants[32] (Fig. 3a and Supplementary Fig.
183 3b). TOLLIP contains three known functional domains: TBD (Tom1 binding), C2
184 (phosphatidylinositol binding) and CUE (ubiquitin binding)[32,33,34,35] (Fig. 3a). WT Tollip and
185 Δ229-274 (lacking CUE) bound KSR1 efficiently. However, Δ180-274 did not, indicating that the
186 "linker" region between C2 and CUE (residues 179-229) is required for this association. The 179-

187 229 sequence displays marked evolutionary preservation among vertebrates, particularly an 18 aa
188 core (185-202) that is nearly perfectly conserved (Supplementary Fig. 3c). Δ203-274, which adds
189 residues 179-202 to Δ180-274, restored the Tollip:KSR1 interaction while a mutant lacking only
190 residues 180-202 (Δ180-202) lost nearly all KSR1 binding (Fig. 3a). Thus, the invariant sequence
191 between C2 and CUE is essential for KSR1 association. A human TOLLIP structure predicted by
192 AlphaFold2.0[36] shows a β-hairpin fold corresponding to the conserved 185-202 segment (Fig. 3b).
193 This structure is absent in the model for *C. elegans* Tollip, which lacks this sequence. The precise
194 alignment of the β-hairpin with the 185-202 motif implies that it has a key role in KSR1 binding.
195 A set of Tollip mutants fused to GFP was analyzed for subcellular localization in A549 cells.
196 WT Tollip was consistently perinuclear, while each mutant (Δ229-274, Δ180-274, Δ1-54, Δ180-
197 202, and Δ55-179) was more broadly distributed in the cytoplasm (Fig. 3c). All deletions except
198 Δ180-202 impinge on functional domains involved in endosome binding (C2), trafficking (TBD)
199 or ER tethering (CUE) and thus are expected to influence perinuclear localization. Deletion of the
200 KSR1 binding region (Δ180-202) was not anticipated to affect perinuclear targeting. It is possible
201 that resection of the linker region alters folding or accessibility of the flanking C2 and/or CUE
202 domains, thus contributing to the observed localization defect.
203

204 ***TOLLIP* is a dependency gene specific to KRAS-driven cancers**

205 As TOLLIP depletion is toxic to *KRAS* mutant tumor cells (Fig. 2), we asked if TOLLIP
206 dependency is specific to *KRAS* cancers or is generally required by transformed cells. Using NIH
207 3T3 cells transformed by $KRAS^{G12V}$ or $HRAS^{G12V}$, we monitored CK2α and KSR1 localization
208 before and after Tollip knockdown. Both *RAS* oncogenes induced perinuclear translocation of
209 CK2α, KSR1 and Tollip in shCtrl cells (Fig. 4a and Supplementary Fig. 4a). Tollip depletion led

210 to pan-cytoplasmic redistribution of CK2α and KSR1 in NIH 3T3^{KRAS} cells but had little effect in
211 HRAS^{G12V}-transformed cells (Fig. 4a). The impact on PSCs correlated with cell proliferation, as
212 Tollip loss decreased the growth rate of NIH 3T3^{KRAS} cells (Supplementary Fig. 4b) but not NIH
213 3T3^{HRAS} cells (Supplementary Fig. 4c). Proliferation of non-transformed NIH 3T3 cells was
214 unaffected by Tollip silencing (Supplementary Fig. 4b,c). Similar results were seen for *Tollip*$^{-/-}$
215 MEFs, which carried an immortalizing *p19*^{Arf} mutation to permit transformation by oncogenic
216 RAS (Supplementary Fig. 4d,e). Growth of *KRAS*^{G12V}-expressing *Tollip*$^{-/-}$ MEFs was reduced to
217 that of non-transformed cells, whereas *HRAS*^{G12V}-tranformed cells were resistant to Tollip
218 deficiency. Consistent with these results, human T24 bladder carcinoma cells (*HRAS*^{G12V})
219 proliferated normally in the absence of TOLLIP and CK2α and KSR1 remained fully perinuclear
220 (Fig. 4b,c). Thus, *KRAS*-driven PSC formation and increased proliferation require TOLLIP, while
221 *HRAS*-transformed cells are TOLLIP independent.

222 We next compared the effect of TOLLIP depletion across a panel of human tumor cell lines
223 harboring various *RAS* pathway oncogenes. Four *KRAS* and two *NRAS* mutant cell lines showed
224 severely reduced clonogenic growth upon TOLLIP silencing (Fig. 4d). However, RL95-2
225 endometrial carcinoma (*HRAS*^{Q61H}), T24 (*HRAS*^{G12V}), A375 melanoma and HT29 colon carcinoma
226 (*BRAF*^{V600E}), OVCAR-8 ovarian carcinoma (*HER2*^{G776V}) and PC3 prostate cancer (*PTEN/TP53*
227 null) cells were unaffected by TOLLIP knockdown (Supplementary Fig. 5a). These different
228 responses did not correlate with TOLLIP protein levels, which were comparable in the various cell
229 lines (Supplementary Fig. 5b). Thus, tumor cells with *KRAS* or *NRAS* mutations are selectively
230 dependent on TOLLIP. Since CK2 PSCs are induced by oncogenic *HRAS* in NIH 3T3 cells and
231 are also present in human tumor cells carrying oncogenes other than *K/NRAS*, another endosomal
232 adaptor(s) likely provides a redundant ER tethering function in these cells.

233

234 **Characterization of a TOLLIP-dependent transcriptome in tumor cells**

235 To further define TOLLIP-regulated cellular processes, we used RNA-seq to compare the
236 transcriptomes of control and TOLLIP-depleted A549 cells (Supplementary Fig. 5c;
237 Supplementary Table 1). Genes that decreased upon TOLLIP knockdown were highly correlated
238 with gene ontology (GO) processes for cell cycle, DNA replication and chromosome segregation
239 (Supplementary Fig. 5d; Supplementary Table 2). Related categories were also identified through
240 gene set enrichment analysis (GSEA; suppressed processes) (Supplementary Fig. 5e;
241 Supplementary Table 3) and include several genes encoding subunits of the MCM helicase
242 complex regulating initiation of DNA replication. This effect may be related to the identification
243 of MCM2 as a potential TOLLIP-dependent CK2 substrate as well as decreased phosphorylation
244 of cyclin-dependent kinase (CDK) targets in TOLLIP-depleted cells (see below). Specifically,
245 reduced MCM2 phosphorylation/activity[37,38] and diminished CDK signaling could impair the
246 onset of DNA replication and subsequent expression of S-phase MCM genes. Predominant
247 upregulated processes were inflammatory response and immune response (Supplementary Fig. 5f
248 and Supplementary Table 3), possibly reflecting cellular stress and senescence elicited by TOLLIP
249 depletion and consistent with TOLLIP's role in regulating pro-inflammatory signaling[39].

250

251 **Tollip facilitates progression to adenocarcinoma in a *Kras^{G12D}*-driven model of lung cancer**

252 To investigate whether Tollip deficiency impairs *Kras*-induced tumor development *in vivo*, we
253 produced *Tollip*$^{-/-}$ mice[41] carrying a Cre-activated *LSL-Kras^{G12D}* oncogene[42]. Ad.Cre virus was
254 administered to the lungs of *WT* or *Tollip* null *LSL-Kras^{G12D}* mice and animals were maintained
255 until disease endpoint. All mice eventually succumbed to respiratory distress due to accumulated

256 pulmonary lesions, and no survival difference was observed between genotypes (P=0.40; Log-rank
257 test) (Fig. 5a). Lung lesions in this model are primarily benign alveolar hyperplasia and adenomas,
258 a few of which advance to malignant ADC (Fig. 5b). Hyperplastic areas (Fig. 5c) and adenoma
259 counts (Fig. 5d) were similar between genotypes, with high adenoma burdens accounting for the
260 similar mortality rates between the two strains. However, carcinomatous lesions were significantly
261 reduced in *Tollip*$^{-/-}$ mice (Fig. 5d). ADCs were the highest tumor grade observed in 83.33% of
262 *Tollip*$^{+/+}$ mice, whereas only 42.1% of *Tollip*$^{-/-}$ animals presented with carcinomas (P=0.017;
263 Fisher's exact test) (Fig. 5e). These findings reveal a significant block to *Kras*-driven ADC
264 development in mutant animals, indicating an important role for Tollip in malignant progression.
265 A previous study reported that Tollip deficiency caused a reduction in colitis-associated colon
266 cancers, which are primarily adenomas[40]. This was attributed to diminished inflammation and
267 reduced infiltration of CD4+/Foxp3+ regulatory T cells and other immune cells. Using CD45 as a
268 pan-immune marker, we did not observe differences in overall immune cell infiltration between
269 *WT* and *Tollip*$^{-/-}$ lung adenomas or ADCs (Fig. 5f), suggesting that the cancer phenotype involves
270 tumor-cell-intrinsic Tollip deficiency. To further address the tumor-cell-autonomous role of
271 Tollip, we delivered TOLLIP-depleted A549 cells intravenously into immunodeficient mice.
272 Whereas cells expressing a control shRNA formed an average of 80 lung lesions per animal, two
273 different shTOLLIP constructs almost completely prevented tumor formation and most animals
274 presented no detectable lesions (Fig. 5g). Thus, human lung ADCs are highly dependent on
275 TOLLIP for tumor engraftment.
276
277 **Phosphoproteomic analysis identifies targets of perinuclear CK2 and other kinases**

278 The presence of oncogenic kinases such as CK2 on perinuclear endosomes suggests they access a
279 specific set of substrates at this location to generate a pro-oncogenic phosphoproteome. Thus, we
280 sought to identify phospho-sites (p-sites) that require TOLLIP or otherwise correlate with PSC
281 formation. We first characterized TOLLIP-dependent modifications by comparing the
282 phosphoproteomes in control and TOLLIP-depleted A549 cells. Phosphopeptides (p-peptides)
283 were isolated by TiO_2 enrichment and analyzed by LC-MS/MS. Intensities of individual p-sites
284 were determined by summing the values for all p-peptides that contain a particular p-site and
285 normalizing to total levels of each protein (Fig. 6a). Altogether, 1513 normalized p-sites were
286 detected (Supplementary Table 4).

287 Ratios of p-site intensities in TOLLIP-depleted vs. control cells were used to generate Z-
288 scores for each p-site. We applied a Z<-1.5 cutoff, as has been used previously[41], to define a set of
289 109 TOLLIP-dependent p-sites (Supplementary Table 4). IPA analysis of these sites revealed one
290 network containing a CK2 node and another with a CDK node (Supplementary Fig. 6a;
291 Supplementary Table 5). GO analysis (Biological Process) showed that the 109 corresponding
292 proteins clustered functionally around chromatin organization and transcription (Fig. 6b;
293 Supplementary Table 6). The Z<-1.5 p-sites were also analyzed for similarity to CK2
294 phosphorylation motifs and were considered matches if they passed at least one of two rules
295 specifying acidic residues in the surrounding sequence[41,42] (see Methods). Eight sites scored as
296 putative CK2 motifs (Fig. 6c; Supplementary Table 4). These proteins were functionally enriched
297 for apoptosis (SH3KBP1 and PDCD4) (Fig. 6d; Supplementary Table 6), consistent with increased
298 death of TOLLIP-depleted cells (Fig. 2c).

299 We also noted a high frequency of CDK motifs in TOLLIP-dependent p-sites. Of the 1513 p-
300 sites in the total A549 data set, 158 (10.44%) were predicted to be CDK sites, while 30 of the 109

301 Z<-1.5 p-sites (27.52%) scored as potential CDK motifs (Supplementary Fig. 6b,c; Supplementary
302 Table 4). The TOLLIP-dependent Z<-1.5 p-sites were enriched for putative CDK targets when
303 compared to all p-sites (P=5.18E-07). The corresponding proteins are functionally associated with
304 chromatin structure and transcription (GO BP) (Supplementary Fig. 6d; Supplementary Table 6).
305 It remains to be determined whether CDK:cyclin complexes are present on TOLLIP-dependent
306 perinuclear endosomes, or if CDK p-sites are down-regulated through an indirect effect of TOLLIP
307 knockdown.

308 As an alternative approach to identifying substrates of perinuclear kinases, we used serum-
309 stimulated NIH 3T3 cells to exploit the temporal features of growth factor (GF)-induced PSC
310 formation. In this model, CK2α becomes perinuclear at 4 and 6 h post-stimulation while p-ERK
311 re-localizes at 6 h[17] (Fig. 6e). Phosphoproteomic analysis was performed on NIH 3T3 lysates
312 harvested at 0, 0.5, 2, 4, 6 and 8 h after GF stimulation and normalized p-site intensities were
313 determined (Supplementary Table 7). To identify p-sites that increase at 4 and/or 6 h, the values
314 at these time points were divided by the combined average of p-site intensities at 0, 0.5 and 2 h.
315 Applying a Z>1.5 threshold revealed 190 p-sites increasing at 4 h and 146 at 6 h (Supplementary
316 Table 7; Supplementary Fig. 6e); these p-sites were significantly enriched for predicted CK2 sites
317 (Fig. 6f). IPA networks based on the 4 h data showed one with a CK2 node and one with a CDK
318 node (Supplementary Fig. 6f; Supplementary Table 8). Filtering for predicted CK2 p-sites revealed
319 77 sites upregulated at 4 h and 53 at 6 h, of which 27 were common (Fig. 6g; Supplementary Table
320 7). Considering all p-sites with Z>1.5, the corresponding proteins at both 4 and 6 h were enriched
321 for mRNA processing and RNA splicing (Supplementary Fig. 6g,h; Supplementary Table 9). The
322 4 and 6 h CK2 p-site-containing proteins also showed associations with RNA processing and
323 rRNA transcription (Supplementary Fig. 6i,j). These results indicate that perinuclear CK2

signaling endosomes appearing during mid-G1 phase in normal cells phosphorylate proteins involved in RNA metabolism, protein synthesis and chromatin structure/transcription.

TOLLIP-dependent perinuclear CK2 phosphorylates the atypical kinase RIOK1 and controls its pro-oncogenic activity

One of the proteins identified as a likely substrate for perinuclear CK2 is the non-canonical protein kinase, RIOK1. RIOK1 was phosphorylated on a predicted CK2 site, $SpS^{22}DSE$, at 4 h in GF-stimulated NIH 3T3 cells (Supplementary Table 7). RIOK1 plays a key role in ribosome biogenesis and is required for processing of the 18S-E pre-rRNA to the mature 18S form[43]. It also controls assembly/maturation of the 40S ribosomal subunit[44,45,46] and thus is an important regulator of protein synthesis. *RIOK1* is a synthetic lethal gene in *KRAS* mutant cancers[47] and is essential for viability of various tumor cell lines[48] and cancers[49]. Moreover, RIOK1 Ser22 has been implicated as a CK2 site[50] and is conserved among mammalian RIOK1 homologs (Fig. 7a). Thus, we asked whether pSer22 is a functionally relevant target of perinuclear CK2 in tumor cells.

To monitor RIOK1 phosphorylation we generated an affinity-purified pSer22 antibody. The antibody recognized over-expressed WT (Ser22) RIOK1 but not S22A, and pSer22 levels increased approximately two-fold upon co-expression with $KRAS^{G12V}$ (Fig. 7b). Endogenous pSer22 was detected in A549 cell lysates and antibody recognition was abolished by incubating lysates with λ-phosphatase (Supplementary Fig. 7a) or treating cells with the CK2 inhibitor, CX-4945 (Supplementary Fig. 7b). Efficient phosphorylation required TOLLIP, as pSer22 signals in A549 cells were reduced by at least 60% following TOLLIP depletion (Fig. 7c). Similar results were observed in PANC1 cells (Supplementary Fig. 7c). Conversely, TOLLIP ablation had no effect on pSer22 levels in *HRAS* mutant T24 cells (Fig. 7d), consistent with the retention of

347 perinuclear CK2 upon TOLLIP knockdown in these cells. These results indicate that Ser22 is an
348 authentic CK2 site whose phosphorylation requires CK2 PSCs.

349 A549 cells displayed acute dependence on RIOK1 in clonogenic growth assays (Fig. 7e),
350 providing a system for assessing the biological activity of RIOK1 Ser22 mutants. Expression of
351 exogenous WT RIOK1 partially restored colony formation, while S22A did not. However, the
352 phosphomimetic S22D variant rescued RIOK1-depleted cells at least as efficiently as WT RIOK1,
353 indicating that Ser22 phosphorylation stimulates RIOK1 activity to support cell growth/survival.

354 RIOK1-dependent 18S-E pre-rRNA processing can be monitored by analyzing levels of the
355 5' internal transcribed spacer 1 (5'ITS1) in the precursor RNA. When processing is impaired, 18S-
356 E precursors accumulate in the cytoplasm[44] (Supplementary Fig. 7d). Using RNA FISH, we
357 confirmed that RIOK1 depletion in A549 cells increased cytoplasmic 5'ITS1 signals (Fig. 7f).
358 TOLLIP knockdown similarly augmented cytoplasmic 5'ITS1 levels, comparable to the effect of
359 RIOK1 depletion. These findings support a pathway whereby TOLLIP-dependent, CK2-mediated
360 phosphorylation on RIOK1 Ser22 is necessary to facilitate 18S rRNA processing and 40S
361 ribosome biosynthesis, contributing to the fitness of *K/NRAS* mutant tumor cells.

362

363 **Discussion**

364 This study demonstrates that tumor cells require translocation of signaling endosomes to the
365 perinuclear ER network. RAB11A$^+$ endosomes containing CK2 and KSR1, but not ERK1/2, rely
366 on TOLLIP for partitioning to the ER. In TOLLIP-depleted tumor cells, CK2, KSR1 and RAB11a
367 revert to a dispersed subcellular distribution resembling that of non-transformed cells, indicating
368 that perinuclear targeting of CK2 and other kinases is a key feature of cancers. TOLLIP was
369 originally identified as a negative regulator of pro-inflammatory signaling[33] but has not been linked

370 to the RAS pathway in tumor cells. Our demonstration that the ER tethering function of TOLLIP[20]
371 is essential for oncogenic signaling in neoplastic cells uncovers an important new function for this
372 adapter beyond its currently known roles[39,51,52,53].

373 TOLLIP recruits KSR1:CK2 complexes to endosomes by binding to KSR1 through a short,
374 conserved region adjacent to the CUE domain that forms a predicted β-hairpin. While the function
375 of this "linker" region was previously unknown, it was recently shown to mediate the association
376 of TOLLIP and STING (stimulator of interferon genes), stabilizing STING and maintaining
377 cGAS-STING signaling in response to microbial pathogens[54]. It will be of interest to determine if
378 binding of KSR1 and STING to the TOLLIP "linker" region is mutually exclusive and whether
379 TOLLIP's role in inflammatory signaling is mechanistically distinct from perinuclear targeting of
380 CK2/KSR1 complexes in cancer cells.

381 The endosome:ER tethering function of TOLLIP is critical for CK2 signaling in a subset of
382 tumor cells, whereas in non-transformed cells PSCs form transiently in response to GF
383 stimulation[17] and cell proliferation/viability is largely unaffected by TOLLIP depletion. *KRAS*-
384 and *NRAS*-transformed cells, irrespective of the *K/NRAS* activating mutation, are highly dependent
385 on TOLLIP for proliferation and survival. In contrast, tumor cells carrying mutant *HRAS*, *BRAF*
386 and other oncogenes are unaffected by TOLLIP loss. The latter cells nonetheless display
387 perinuclear partitioning of CK2 and KSR1 that is impervious to TOLLIP depletion. These findings
388 point to the existence of alternative pathways for PSC formation involving different endosomal
389 adaptors. Adding further complexity, ERK1/2 kinases are associated with a distinct class of
390 signaling endosomes that lack TOLLIP, with ERK remaining perinuclear in TOLLIP-depleted
391 cells. Moreover, a recent study showed that EGF stimulation causes PI3K to migrate intracellularly
392 along microtubules, leading to AKT activation at perinuclear endosomes rather than at the plasma

393 membrane[55]. Thus, it is possible that active AKT also resides on ER-anchored endosomes. Future
394 work will seek to identify other endosomal oncogenic kinases and adaptors that establish the full
395 spatial signaling landscape in tumor cells, including the adapter that acts redundantly to TOLLIP
396 in non-*K/NRAS* mutant cancers. We observed a pronounced decrease in CDK p-sites upon TOLLIP
397 silencing, raising the possibility that certain CDKs may be associated with TOLLIP^{+} endosomes.
398 However, this result must be interpreted with caution as it could arise from an upstream cell cycle
399 block that secondarily prevents CDK activation. Further studies are needed to determine whether
400 active CDKs are present on perinuclear endosomes.

401 Our findings implicate PSCs as critical signaling engines in cancers, generating an onco-
402 phosphoproteome required to meet the demands of increased cell proliferation, altered metabolism
403 and pro-apoptotic stresses. p-sites whose phosphorylation corresponds to perinuclear CK2 were
404 found in proteins regulating translation (eIF4B and PDCD4) and ribosome biogenesis (RIOK1 and
405 nucleolin). Hyperactivation of ribosome biogenesis occurs in cancers and can be driven by
406 oncogenes[56]. Accordingly, oncogenic Kras stimulates the RNA-binding activity of nucleolin
407 through phosphorylation by CK2 on four sites[57], two of which coincide with our GF-stimulated
408 NIH 3T3 data (Supplementary Table 7). These modifications augment the ability of nucleolin to
409 stabilize pre-rRNA transcripts, enhancing ribosome biogenesis. The final step of pre-18S rRNA
410 processing is dependent on RIOK1[43,45,46] and also requires TOLLIP, and the RIOK1 CK2 site
411 (Ser22) was critical for its ability to support proliferation/survival of A549 cells. Taken together,
412 these observations support a model in which ER-tethered CK2 signaling endosomes specify
413 phosphorylation of pro-oncogenic targets such as RIOK1 and nucleolin in tumor cells
414 (Supplementary Fig. 8). To our knowledge, the present study provides the first definitive evidence
415 that subcellular localization of endosome-associated kinases controls their substrate selectivity.

416 Tollip facilitates the development of *Kras*^{G12D}-driven lung ADCs but is dispensable for benign
417 lesions such as neoplasia and adenomas. Progression to carcinoma in *Kras* lung cancer models has
418 been linked to increased MEK-ERK signaling, with high p-ERK levels often associated with
419 amplification of the mutant *Kras* locus[58]. Interestingly, *Kras*-induced adenomas display
420 perinuclear CK2, KSR1[17] and Tollip (Supplementary Fig. 1g) even though these benign lesions
421 develop efficiently in the absence of Tollip. Evidently there is a transition to Tollip dependence
422 that accompanies progression to lung ADC, possibly involving enhanced RAS pathway signaling.
423 Human *KRAS* mutant cell lines are nearly always derived from late-stage malignant carcinomas,
424 which likely explains their TOLLIP addiction. As TOLLIP is an Achilles heel of *KRAS* and *NRAS*
425 tumor cells, it could potentially be exploited as a therapeutic target in these cancers.
426

427 **Acknowledgements**

428 We thank Dr. A. Ciarrocchi for providing *Tollip* constructs, T.N. O'Sullivan for generating KPC
429 pancreatic tumor samples, and A. Kane (Scientific Publications, Graphics & Media, Leidos
430 Biomedical Research, Inc., Frederick National Laboratory for Cancer Research) for assistance
431 with figure preparation. This research was supported in part by the Intramural Research Program
432 of the NIH, National Cancer Institute, Center for Cancer Research, and in part with Federal funds
433 from the National Cancer Institute, National Institutes of Health, under Contract Nos.
434 HHSN261200800001E and 75N91019D00024. Analysis and management of images and
435 associated metadata was supported in part by the NCI HALO Image Analysis Resource. The
436 content of this publication does not necessarily reflect the views or policies of the Department of
437 Health and Human Services, nor does mention of trade names, commercial products, or
438 organizations imply endorsement by the U.S. Government.

Contributions

S.B. and P.F.J. conceived the study and designed experiments. S.B. performed the experiments. B.T.L. and M.G. provided bioinformatic analysis of phosphoproteomic and RNA-seq data, respectively. K.S. and N.M. conducted animal experiments and genotyping. S.K. provided mouse pancreatic tumor samples. B.K. and L.B. performed histopathological analysis of lung tumor samples. S.L. devised the method to calculate RNPI and implemented it in a Fiji macro script. S.D. and T.A. designed and performed mass spectrometry experiments and data analysis. D.E. provided key plasmid constructs. S.B. and P.F.J. wrote the manuscript with input from all authors.

Methods

Animal experiments

Mice were maintained in accordance with NIH animal guidelines following protocols approved by the NCI-Frederick Animal Care and Use Committee. Mouse embryonic fibroblasts (MEFs) were isolated from *WT*, *Tollip*$^{-/-}$[53], *p19*$^{Arf-/-}$ and *p19*$^{Arf-/-}$*;Tollip*$^{-/-}$ E13.5 mouse embryos (C57Bl/6Ncr strain background), and cells were maintained at low passage. *Kras*^{LA2}/+[59], *LSL-Kras*^{G12D}/+[60] and *Tollip*$^{-/-}$*;LSL-Kras*^{G12D}/+ mice (C57Bl/6Ncr background) were used for tumor studies. To induce lung tumors in *LSL-Kras*^{G12D} strains, Ad.Cre virus (Viral Vector Core Facility, University of Iowa College of Medicine) was administered by intratracheal instillation of 1.5 or 3.0x10^7 pfu/animal. Animals that became moribund (thin, hunched, labored breathing, rough coat, or lethargy) were sacrificed, lungs were removed and fixed in 10% Neutral Buffered Formalin (NBF) and embedded in paraffin blocks. Lungs from normal mice were used as controls. NBF fixed paraffin-embedded pancreatic tumor tissue sections were obtained from KPC mice (*Pdx-1-Cre (B6.Tg(Pdx1-cre)6Tuv/Nci*); *LSL-Kras*^{G12D} (*B6.Krastm4Tyj/Nci*); *LSL p53*^{R172H} *(129S4-Trp53tm2Tyj/Nci)* on a

462 C57BL/6 background)[61]. Pancreas samples from *WT* mice were used as controls. Primary tumor
463 cell line KPC98027 was derived from a KPC pancreatic ductal ADC. $1x10^5$ KPC cells were
464 injected into medial pancreata in syngeneic C57BL/6 recipient animals. Pancreas from un-injected
465 normal mice were used as controls. Tumors were collected at 5-6 weeks post-injection and fixed
466 in NBF as described above. For xenograft experiments, athymic nude (*nu/nu*) mice received 1×10^6
467 A549 cells (control or TOLLIP knockdown) by tail vein injection. All mice were sacrificed when
468 a single mouse showed clinical signs and became moribund. Lungs were removed and lesions
469 counted. Lungs were gently inflated in NBF, fixed with NBF for 5 days and embedded in paraffin
470 blocks or stored in 70% ETOH.
471
472 **H&E staining, tumor grading and HALO AI-based image analysis of lung tumor slides**
473 Mouse lungs were formalin-fixed, embedded in paraffin and sectioned at 5µm thickness. Routine
474 hematoxylin and eosin-staining was performed using the Sakura® Tissue-Tek® Prisma™
475 automated stainer (Sakura Finetek USA, Inc., Torrance, California). The slides were dewaxed
476 using xylene and then hydrated using a series of graded ethyl alcohols. Commercial hematoxylin,
477 clarifier, bluing reagent and eosin-Y were used to stain. A regressive staining method was used,
478 which intentionally overstains tissues and then uses a differentiation step (clarifier/bluing reagents)
479 to remove excess stain. After staining was completed, the slides were cover slipped using the
480 Sakura® Tissue-Tek™Glass® automatic cover slipper (Sakura Finetek USA, Inc., Torrance,
481 California). Whole slide images were obtained at high resolution, 20x magnification using an AT2
482 scanner (Aperio, Leica Biosystems, Buffalo Grove, IL, USA).
483 Two veterinary pathologists (B.K. and L.B.) identified and segmented the regions of interest
484 used to train an AI deep learning tissue-classifying algorithm (Densenet AI V2 plugin in Halo

485 (v.3.3.2541.423, Indica Labs, Corrales, NM, USA). Annotations were manually drawn around four
486 tissue classes: normal (including lung parenchyma, airways and vessels), hyperplasia
487 (hypercellular foci of round to cuboidal hypertrophic pneumocytes arranged in a single layer),
488 adenoma (expansile mass consisting of proliferative epithelium arranged in papillary to solid
489 formations with no features of atypia and rare to absent mitotic figures), and adenocarcinoma
490 (proliferative cells demonstrating some combination of increased cellular atypia, anisocytosis,
491 anisokaryosis, cytoplasmic basophilia, increased mitotic figures and haphazard or invasive
492 patterns).

493 During training, the algorithm performance was iteratively evaluated by visual inspection and
494 misclassification of tissues was addressed and corrected by additional annotations in the
495 misclassified regions and further training until satisfactory performance was obtained. The
496 percentages of lungs comprised of hyperplasia, adenoma and adenocarcinoma were calculated by
497 dividing the total area of each class by the total tissue area on the slide and multiplying by 100.

498

499 **Immunohistochemistry**

500 Immunohistochemical staining for CD45 was performed on 5-micron FFPE sections using a
501 manual benchtop method. Antigen retrieval was performed with citrate buffer for 30 seconds at
502 121°C using a Decloaking Chamber (BioCare Medical). Nonspecific binding was blocked with an
503 incubation of 2% normal rabbit serum for 20 min. This was followed by an overnight incubation
504 at 4°C with the CD45 primary antibody (BD Biosciences #550539) at a 1:100 dilution. Antibody
505 detection was accomplished by incubation with Biotinylated Rabbit anti-Rat (Vector labs# BA-
506 4001) secondary antibody and ABC Elite reagent (Vector Labs # PK-6100), followed by

507 incubation in DAB chromogen (Sigma #D5905). Slides were digitally scanned at 20x using a Leica
508 AT2 whole slide scanner. Normal mouse spleen was used a positive control.
509 Regions having adenoma and adenocarcinoma lesions were graded as mentioned above using
510 Halo AI on the H&E slides, and CD45 staining in the corresponding regions was analyzed.
511 Hematoxylin nuclear stain was used as a marker to count the total number of cells within the graded
512 adenoma or adenocarcinoma lesions. The percentage of CD45 stained cells was plotted.
513

514 **Cells and cell culture**

515 HEK-293T cells (American Type Culture Collection (ATCC), Rockville, MD) and MEFs were
516 cultured in DMEM+Glutamax (supplemented with 10% Fetal Bovine Serum (FBS). HBEC cells
517 (ATCC) were cultured in Airway Epithelial Cell Basal Medium (ATCC® PCS-300-030)
518 supplemented with Bronchial Epithelial Cell Growth Kit (ATCC PCS-300-040). NIH3T3 cells
519 were grown in DMEM+Glutamax with 10% calf serum (Colorado Serum Company). A549
520 (ATCC) cells were grown in Ham's F-12K (Kaighn's) medium with 10% FBS. PANC-1, A375,
521 MDA-MB-231, HepG2 and MIA PaCa-2 cells (ATCC) were grown in DMEM+Glutamax with
522 10% FBS. PC-3, OVCAR-8 and NCI-H1299 cells (ATCC) were grown in RPMI+Glutamax with
523 10%FBS. KPC98027 cells were cultured in DMEM/F12+Glutamax with 10% FBS. *HRAS* mutant
524 cancer cell lines T24 and RL95-2 were kindly provided by Dr. Deborah Morrison (NCI-Frederick)
525 and were grown in McCoy's 5A and DMEM/F12+Glutamax, respectively. HT-29 cells were
526 cultured in McCoy's 5A medium with 10% FBS. All media and FBS were obtained from Thermo
527 Fisher Scientific. To prevent Mycoplasma contamination, cell cultures were additionally
528 supplemented with Plasmocin (InvivoGen). Cell stocks were generally passaged fewer than 5

529 times, and freshly thawed cells were maintained in culture for no more than 2 weeks before
530 conducting experiments.
531
532 **Antibodies**
533 Rabbit polyclonal antibodies to TOLLIP (11315-1-AP) and RAB11A (20229-1-AP) were obtained
534 from Proteintech Group. Mouse monoclonal antibody to Tollip (Clone: MAB4678) was obtained
535 from R&D Systems. Rabbit Anti-CSNK2A1 (CK2α) antibody (ab10466) was from Abcam. Rabbit
536 antibodies to phospho-ERK1/2 (#9101) and HA-Tag (#3724) were from Cell Signaling
537 Technologies. Mouse antibodies to β-Actin (sc-47778) and p-ERK1/2 (sc-136521) were obtained
538 from Santa Cruz Biotechnology. Rabbit antibodies to HRAS (GTX-116041) and KSR1
539 (GTX56241) were from GeneTex. Affinity purified mouse antibody against Pyo epitope tag (Glu-
540 Glu) was from BioLegend (#901802). Mouse monoclonal antibody against KRAS (H00003845-
541 M01) was obtained from Abnova. Anti-mouse (W4028) and anti-rabbit (W4018) HRP conjugated
542 secondary antibodies were from Promega. Anti-mouse Alexa® Fluor 488 (#A32790) and anti-
543 rabbit Alexa® Fluor 594 (A-21207) conjugated secondary antibodies were from Thermo Fisher
544 Scientific. A custom phospho-Ser22 RIOK1 polyclonal antibody (Biosynth) was raised in rabbits
545 using the immunogenic peptide H-Cys-Asp-Asp-Ala-Asp-Ser-**p**Ser-Asp-Ser-Glu-Asn-NH2.
546 Peptides were synthesized and purified using high-performance liquid chromatography (HPLC) to
547 >90% purity as determined by HPLC and/or LC/MS. The immunogen was conjugated to activated
548 keyhole limpet hemocyanin (KLH). Two Specific Pathogen Free New Zealand white rabbits (12-
549 16 weeks old) were immunized subcutaneously with the phospho-peptide conjugate. All animal
550 protocols were approved by the Institutional Animal Care and Use Committee. To remove any
551 latent "non-phospho" reactive antibodies, the anti-sera were passed twice through SulfoLink resin

552 (ThermoFisher scientific # 20402) columns coupled to the non-phosphorylated peptide. The final
553 flowthrough was passed through SulfoLink resin coupled to the phosphorylated peptide to obtain
554 affinity-purified phospho-RIOK1 Ser-22 antibodies.
555
556 **Reagents**
557 1 mg/ml stock solution of Doxycycline hyclate (Sigma Aldrich, # D9891-1g) were prepared in
558 distilled water and filter sterilized. The final concentration of Doxycycline (Dox) used was 1µg/ml.
559 CK2 inhibitor, CX-4945 (Silmitaserib) was purchased from Activate Scientific (#AS10115-G1)
560 and λ-phosphatase (λ-PPTase) was obtained from Merck Millipore Sigma (#P9614-20KU).
561 Thapsigargin (T9033, Millipore Sigma) was used at 400nM concentration.
562
563 **Plasmids and lentiviral vectors**
564 *Ksr1* expression plasmids containing an N-terminal Pyo tag (EYMPME) were generated by PCR
565 amplification using pcDNA3 mouse *Ksr1*[62] as a template and inserting fragments into pcDNA3.1.
566 C-terminal deletion mutants 1-81 (CA1), 1-286 (CA1-2) were cloned using EcoRI and BamH1
567 sites, while 1-377 (CA1-3), and 1-479 (CA1-4) were cloned using EcoR1 and Kpn1 restriction
568 sites. N-terminal deletion mutant 531-873 (CA5) was inserted using EcoR1 and BamH1 sites.
569 Expression plasmids for HA-tagged WT rat *Tollip* and deletion mutants (Δ229-274, Δ180-274,
570 Δ1-54 and Δ1-94) in pRK7[32] were a kind gift from Dr. A. Ciarrocchi (Laboratory of Translational
571 Research, Azienda Unità Sanitaria Locale-IRCCS di Reggio Emilia, Italy). HA-*Tollip* deletion
572 mutant Δ203-274 was made by PCR amplification and cloning into the pRK7 vector using BamH1
573 and EcoR1 restriction sites. Δ180-202 was made using three-way ligation of cDNA fragments
574 encoding *Tollip* residues 1-179 and 203-274, and BamH1/EcoR1 digested pRK7 vector; Nhe1 sites

575 were used to join the two *Tollip* cDNA fragments. pLenti CMV GFP Hygro (656-4) was a gift
576 from Eric Campeau and Paul Kaufman (Addgene plasmid #17446; http://n2t.net/addgene:17446;
577 RRID:Addgene_17446)[63]. Rat WT *Tollip* and deletion mutants Δ229-274, Δ180-274, Δ1-54,
578 Δ180-202 were cloned into pLenti CMV GFP Hygro using PCR amplification from the pRK7
579 based Rat *Tollip* plasmids mentioned above, using primers containing BsrG1 and Sal1 sites. Δ55-
580 179 was made using three-way ligation of cDNA fragments encoding *Tollip* residues 1-54 and
581 180-274, and BsrG1/Sal1 digested pLenti CMV GFP Hygro vector; Nhe1 sites were used to join
582 the two *Tollip* cDNA fragments. Human *TOLLIP* was amplified from cDNA isolated from A549
583 cells using primers containing BsrG1 and Sal1 sites and the product inserted into pLenti CMV
584 GFP hygro vector. A BsrG1 site within the *TOLLIP* cDNA was eliminated by mutation while
585 maintaining the amino acid sequence, using the QuikChange Lightning Site-Directed Mutagenesis
586 Kit (Agilent, #210518) per the manufacturer's instructions. Lentiviral Rat *Tollip* constructs
587 containing C-terminal fusion to EGFP were generated using three-way Gateway cloning. The
588 minimal CMV promoter-containing pDONR258 and C-terminal m-EGFP tag-containing
589 pDONR257 were obtained from the NCI RAS Initiative (Leidos Biomedical Research, Inc.,
590 Frederick, MD, USA). Coding sequences for Rat *Tollip* WT and deletion mutants were PCR
591 amplified from the corresponding pLenti CMV GFP hygro vectors (described above) and cloned
592 into pDONR255. The CMV promoter, either Rat *Tollip* WT, Δ229–274, Δ180-274, Δ1-54, Δ180-
593 202 or Δ55-179 coding regions, and m-EGFP were then inserted into the lentiviral pDest659 vector
594 (carrying Blasticidin resistance and attR4/attR3 recombination sites). The resulting *Tollip* WT or
595 deletion mutant vectors were used for viral production and transduction. Lentiviral expression
596 vectors for GFP- or mCherry-tagged human *KSR1*, mCherry-tagged mouse *Ck2α*, and FLAG-
597 tagged human *RIOK1* were obtained from Genecopoeia (Rockville, MD). Lentiviral *RIOK1*

598 constructs were generated using four-way Gateway cloning. The minimal CMV promoter-
599 containing pDONR259 vector and the 3X-FLAG tag containing pDONR235 vector were obtained
600 from the NCI RAS Initiative (Leidos Biomedical Research, Inc., Frederick, MD, USA). The
601 human WT *RIOK1* coding region was PCR amplified from cDNA isolated from A549 cells; oligos
602 containing the RIOK1 polyadenylation signal (PAS) were annealed. *RIOK1* coding region and
603 *RIOK1* PAS fragments were then cloned into pDONR255 and pDONR257 vectors, respectively,
604 using BP recombination. The *RIOK1* Ser22 to Ala (A) or Ser22 to Aspartate (D) mutants were
605 generated using QuikChange Lightning Site-Directed Mutagenesis Kit (Agilent, Catalog
606 #210518). Primers were designed using the QuikChange Primer Design website. Using four-way
607 LR recombination, the CMV promoter, 3X-FLAG, either WT, S22A or S22D *RIOK1* coding
608 regions, and the *RIOK1* PAS fragment were cloned into the lentiviral pDest659 vector. The
609 resulting *RIOK1* WT, S22A or S22D vectors were used for either transfection or viral production
610 and transduction. Lentiviral vectors for human $HRAS^{G12V}$ and $KRAS^{G12V}$ were obtained from the
611 NCI RAS Initiative (Leidos Biomedical Research, Inc., Frederick, MD, USA). Lentiviral
612 packaging/envelope plasmids pMD2.G (#12259), pMDLg/pRRE (#12251), and pRSV/Rev
613 (#12253) were obtained from AddGene. pLV-ER GFP encoding GFP-tagged *SEC61β* was a gift
614 from Pantelis Tsoulfas (Addgene plasmid #80069; http://n2t.net/addgene:80069;
615 RRID:Addgene_80069). mEmerald-RAB11A-7 was a gift from Michael Davidson (Addgene
616 plasmid #54245; http://n2t.net/addgene:54245; RRID:Addgene_54245). pTag-RFP-C-h-Rab11a-
617 c-Myc was a gift from James Johnson (Addgene plasmid #79806; http://n2t.net/addgene:79806;
618 RRID: Addgene_79806)[64]. The lentiviral pUltra-hot vector was a gift from Malcolm Moore
619 (Addgene plasmid #24130; http://n2t.net/addgene:24130; RRID: Addgene_24130). mEmerald
620 tagged human *RAB11A* and RFP tagged human *RAB11A* were transferred into the Ultra-hot vector

621 using Age1 and BamH1 cloning sites. Similarly, mCherry tagged human *TOLLIP* was cloned into
622 the Ultra-hot vector. Mission shRNA lentiviral constructs for human *TOLLIP* (TRCN0000314717,
623 TRCN0000356024 and TRCN0000314642), mouse *Tollip* (TRCN0000066136 and
624 TRCN0000066137), human *RAB11A* (TRCN0000073022 and TRCN0000291939) and human
625 *KSR1* (TRCN0000338414 TRCN0000338476) were obtained from Millipore Sigma.
626 SMARTvector Inducible Human RIOK1 hEF1a-TurboGFP shRNAs [#V3SH11252-224914513
627 (i-shRIOK1.3) and #V3SH11252-229953481(i-shRIOK1.4)], were obtained from Dharmacon
628 (Horizon Discovery). All oligonucleotide primers used in cloning procedures are shown in
629 Supplementary Table 10.
630

631 **Transient transfection**

632 Transfections were carried out using FuGENE 6 transfection reagent (Promega #E2691) per the
633 manufacturer's instructions. Briefly, HEK293T cells in 100mm dishes were transfected with
634 varying amounts of Pyo-tagged *Ksr1* or deletion mutants (standardized to obtain equivalent protein
635 expression), HA-tagged *Tollip* or *Tollip* deletion mutants (standardized to obtain equivalent
636 protein expression), or 2µg of FLAG-tagged human *RIOK1* or *RIOK1* S22A with or without 0.1µg
637 pcDNA3-$KRAS^{G12V}$. Empty pcDNA3 was added when necessary to equalize total vector DNA. 2µl
638 FuGENE 6 transfection reagent per µg of DNA was used for each transfection. Transfection mix
639 was made in antibiotic free Opti-MEM medium (Thermo Fisher Scientific, Catalog #11058021).
640 After transfection, cells were cultured in complete media (DMEM with 10% FBS) for 24 h. Media
641 was changed, and cells were incubated for another 24 h before harvesting. For experiments
642 involving $KRAS^{G12V}$, media was changed 24 h after transfection and cells were incubated for 12

643 h in complete media followed by overnight incubation in low serum conditions (DMEM with 0.1%
644 FBS) prior to harvesting.
645
646 **Lentiviral transduction**
647 Lentiviral plasmids were transfected into 293T cells using a standard $CaPO_4$ precipitation method
648 with 20 µg lentiviral vector, 6 µg pMD2.G, 10 µg pMDLg/pRRE and 5 µg pRSV/Rev. After 24 h,
649 cells were washed with phosphate-buffered saline (PBS) and supplemented with fresh media. 48-
650 72 h after transfection, viral supernatants were collected, pooled, filtered through 0.45 mm filters,
651 supplemented with 8 µg/ml polybrene and used to infect target cells. 24 h later, media was
652 removed, cells washed with PBS and supplemented with fresh media and the appropriate
653 antibiotic. Multiple genes were introduced by sequential infection and drug selection.
654
655 **Growth curves**
656 Cells were seeded at $2.5x10^4$ cells/well in 6-well dishes. At the appropriate times, cells were
657 washed with PBS, fixed in 10% formalin, rinsed with water, stained with 0.1% crystal violet
658 (Millipore Sigma) for 30 min, rinsed extensively, and dried. Dye was extracted with 10% acetic
659 acid and absorbance measured at 590 nm. All values were normalized to day 0 (24 h after plating).
660 Growth curves were plotted using GraphPad Prism 10.2.0.
661
662 **Clonogenic growth assays**
663 4000 cells (A549, PANC1, MDA-MB-231, MIA PaCa-2, H1299, HepG2, RL95-2, A375, HT29,
664 OVCAR-8 and PC3) or 1000 cells (T24) or their respective derivatives were plated on 100 mm
665 culture dishes. After 10-14 days, colonies were fixed with 4% formaldehyde in PBS for 10 min,

666 stained with 0.4% crystal violet for 30 min, rinsed thoroughly with water, dried and scanned. The
667 number of colonies were counted using FIJI/ImageJ software v1.53f51.
668
669 **Senescence-associated β-Galactosidase (SA-βGal) assays**
670 A549 cells or their derivatives were plated at $2.5x10^4$ cells per well in 6-well plates. After 2-3
671 days, cells were stained using a senescence detection kit (Millipore Sigma QIA117) per the
672 manufacturer's instructions.
673
674 **Immunoprecipitation (IP)**
675 $1x10^6$ HEK293T cells were seeded in 10 cm dishes and transfected with DNA combinations using
676 FuGENE6 (Promega) as described above. 48 h after transfection, cells were washed twice with
677 PBS and processed for cell lysis. For IP of endogenous TOLLIP and exogenously expressed pyo-
678 KSR1, non-denaturing Lysis Buffer (137 mM NaCl, 20 mM Tris pH 8.0, 10% glycerol,1% Triton
679 X-100) was used. Lysis buffer supplemented with freshly prepared protease inhibitors (Protease
680 Inhibitor Cocktail Set I #539131 and Protease Inhibitor Cocktail Set III #539134, Millipore Sigma-
681 Aldrich) and phosphatase inhibitors (Phosphatase Inhibitor Cocktail Set I #524624 and
682 Phosphatase Inhibitor Cocktail Set II #524625; Millipore Sigma-Aldrich) was added directly to
683 the plated cells for 15 min on ice. Lysates were centrifuged at 13,000 rpm for 5 min, supernatants
684 collected, and protein estimated using Bradford reagent (Bio-Rad Laboratories, #50000006). 2 mg
685 supernatant was used for immunoprecipitation, with 10% reserved for input samples. For IP of
686 endogenous TOLLIP, cell lysates were pre-cleared by adding 30 µl of a 50% slurry of Protein G
687 Sepharose (GE Healthcare, #17-0618-01) for 1 h. For pre-clearing for pyo-KSR1 IP, 10µl of
688 Protein G magnetic beads (NEB, S1430S) was used. Precleared supernatant was collected either

689 by centrifugation at 1000 rpm or using a magnetic rack (NEB). Anti-TOLLIP or anti-Glu Glu
690 (Pyo) antibody (1:1000) was added to the pre-cleared supernatants and incubated for 1 h at 4°C on
691 a rotating rack. 30µl of 50% slurry of Protein G Sepharose or 10µl Protein G magnetic beads were
692 added and incubated at 4°C on a rotating rack for 1 h. Beads were collected and washed 4 times in
693 NET-N Wash Buffer (100mM NaCl, 20 mM Tris pH 8.0, 1 mM EDTA and 0.5% NP40). 2xSDS
694 sample buffer (Bio-Rad Laboratories) was added to the beads and samples boiled for 7 min at
695 100°C. Proteins were analyzed by immunoblotting as described below.
696

697 **Immunoblotting**

698 Cells were harvested after washing twice with cold PBS and lysed with IP lysis buffer or RIPA
699 lysis buffer supplemented with protease and phosphatase inhibitors (see above for details). Cells
700 were lysed on ice for 15 min. Protein samples (30-50 µg) or IP samples were resolved by
701 electrophoresis on 10% or 12% Mini or Midi-TGX Precast Gels (Bio-Rad Laboratories, Cat. nos:
702 4561034, 4561044, 5671044 and 5671034) and transferred to PVDF membranes (Bio-Rad
703 Laboratories, Cat. no. 1704273). The blots were probed with the appropriate primary antibodies
704 followed by goat anti-rabbit IgG or goat anti-mouse IgG conjugated to horseradish peroxidase and
705 visualized using enhanced chemiluminescence substrate (SuperSignal™ West Dura Extended
706 Duration Substrate #34076, Thermo Fisher Scientific).
707

708 **Live cell imaging**

709 $1x10^4$ cells were plated in glass-bottomed chambers (Sarstedt Cat. no. 94.6190.402) or µ-Slides
710 VI0.4 (Ibidi) and cultured for 24 h. Cells were then infected with supernatants of the appropriate
711 lentiviral vectors. After 18-24 h, media was replaced, and cells were grown in DMEM+10%FBS

712 for 24h. Media was then replaced with DMEM +0.1% FBS and cells cultured overnight. Cells
713 were imaged using a Zeiss LSM-780 confocal microscope equipped with an incubation chamber
714 maintained at 37°C in 5% CO_2.
715
716 **Immunofluorescence (IF)**
717 $1x10^4$ cells were plated in glass-bottomed chambers (Sarstedt, Cat. no. 94.6190.402) or μ-Slides
718 VI0.4 (Ibidi) and cultured for 24 h. Cells were serum starved overnight and fixed with ice cold
719 100% methanol for 20 min. The fixed cells were incubated for 1 h in blocking buffer [5% Normal
720 Goat Serum (Cell Signaling) in PBS with 0.3% TritonX100 (Sigma)]. Thereafter, the cells were
721 incubated with the appropriate primary antibodies (1:1000 dilution) overnight at 4°C in blocking
722 buffer. Following 4 washes with IF wash buffer (PBS containing 1% BSA and 0.1% TritonX100),
723 Alexa 488 or Alexa 594 conjugated secondary antibodies (1:1000 dilution) in IF wash buffer were
724 added for 1 h at RT. The cells were then washed 4 times and stained with 0.1 μg/mL DAPI (Thermo
725 Fisher Scientific) in PBS for 12 min at room temperature followed by 3 washes with PBS.
726 Fluorescence images were acquired using a Zeiss LSM-780 confocal microscope. For IF of tumor
727 samples, dissected tumor-bearing lungs or pancreata embedded in paraffin blocks (described
728 above); were dissected and 5μm sections were prepared and slides processed for
729 immunofluorescence. Briefly, slides were deparaffinized using xylene, rehydrated by treating with
730 sequentially decreasing concentrations of ethanol, and antigen retrieval performed using sodium
731 citrate buffer (10mM sodium citrate, 0.05% Tween 20 and 1M HCl). Thereafter, the slides were
732 washed with PBST, fixed in ice-cold methanol for 10 min at -20°C, permeabilized with 1%
733 TritonX100 for 15 min at RT and 1% SDS for 10 min at RT; all steps were interspersed with 3
734 PBS washes. Slides were blocked using 5% goat serum with 0.3% TritonX-100 in PBS, followed

735 by overnight incubation with rabbit primary antibodies targeting Tollip, KSR1, CK2a or p-ERK
736 at 1:500 dilution in blocking buffer, followed by washing with IF wash buffer (0.1% Triton X-
737 100/1% BSA in PBS) and incubating with Alexa 594 conjugated secondary anti-rabbit antibody
738 (1:500 dilution in IF wash buffer) for 1 h at RT. DAPI staining was performed as described above
739 and the slides were mounted on cover slips using Vecta-shield mounting media
740 (VECTASHIELD® Antifade Mounting Medium, H-1000, VectorLabs). Fluorescence images
741 were acquired using a Zeiss LSM-780 confocal microscope.
742
743 **Fluorescence-based image analysis**
744 Relative nuclear proximity index (RNPI), which measures the proximity of cytoplasmic
745 fluorescence signals to the nuclear envelope, was used to analyze manually selected lateral (XY)
746 confocal slices using FIJI/ImageJ v1.53f51 image analysis software[65]. Using the Differential
747 Interference Contrast (DIC) image and the DAPI stained nucleus, the cell border was traced
748 manually and the nuclear border was drawn around the cell nucleus. Then a Fiji macro (available
749 with instructions from the authors upon request) performed the proximity analysis. The macro first
750 required the user to set a threshold intensity to discriminate punctate fluorescence signals from
751 background intensity. Then the macro automatically made four calculations: (1) The area of the
752 cytoplasm, (2) The total intensity of the fluorescence signals above the manually set threshold
753 intensity (the macro did not subtract the background intensity from the fluorescence signals.), (3)
754 The closest distance to the nuclear border determined for each pixel in the cytoplasm (excluding
755 the nucleus) using the Euclidean distance transform, and then integration of these distance values
756 over the cytoplasm, and (4) The product of the fluorescence intensity above background calculated
757 for each pixel in the cytoplasm [from (2)] and the distance value [from (3)], and then integration

758 of these products over the cytoplasm. The manually set threshold intensity was kept constant in an
759 individual experimental set. The four values from these calculations were used to calculate the
760 average distance of the fluorescence signals from the edge of the nucleus [the value from (4)
761 divided by the value from (2)], and to calculate the average distance a uniform signal in the
762 cytoplasm would have from the edge of the nucleus, which is the value from (3) divided by the
763 value from (1). The ratio of the average distance of the fluorescence signals from the edge of the
764 nucleus to the average distance a uniform signal in the cytoplasm would have from the edge of the
765 nucleus was calculated for each cell. If the ratio is significantly above 1 then the fluorescence
766 signals are further away from the nucleus than a uniformly distributed signal. If the ratio is
767 significantly below 1 then the fluorescence signals are closer to the nucleus than a uniformly
768 distributed signal. RNPI values were plotted using Graphpad Prism 10.2.0.

769 Pearson's correlation coefficient and Manders overlap coefficient (Zen Blue software-based
770 Image analysis tool) were used to determine colocalization between proteins (Pearson's coefficient
771 value quantifies the degree to which fluorescence pixels from two channels follow a simple linear
772 relationship of intensity, while Manders coefficient quantifies the degree of overlap between two
773 fluorescent pixels). The resultant values were plotted using GraphPad Prism 10.2.0.

774

775 **Proximity ligation assay (PLA)**

776 $1x10^4$ A549 cells were grown on glass bottom μ-Slides VI0.4 (Ibidi). PLA was performed using
777 the Duolink *in situ* PLA kit according to the manufacturer's instructions (Millipore Sigma,
778 DUO92002 , DUO92004 and DUO92014). In brief, cells were fixed with pre-chilled MeOH for
779 15 min at -20ºC and permeabilized with 0.05% Saponin in PBS. After blocking, the cells were
780 incubated overnight at 4°C with the appropriate combinations of antibodies. PLA Plus and Minus

781 probes for mouse and rabbit antibodies (used at 1:5 dilution in Duolink® Antibody Diluent) were
782 added and incubated for 1 h at 37°C in a pre-heated humidified chamber. The proximity ligation
783 reaction and the polymerase-based DNA amplification reaction were performed for 30 min and 1
784 h 40 min, respectively, at 37ºC. Samples were counterstained with DAPI for 12 min and images
785 were acquired using a Zeiss LSM-780 confocal microscope. PLA spots were quantified using
786 FIJI/ImageJ software v1.53f51.
787
788 **RNA FISH**
789 1×10^4 A549 cells were plated on μ-Slides VI0.4 (Ibidi). 48 h after seeding, cells were washed in
790 Cytoskeleton buffer (CB; 10 mmol/L MES pH 6.1, 150 mmol/L NaCl, 5 mmol/L $MgCl_2$, 5 mmol/L
791 EGTA, 5 mmol/L glucose) and permeabilized/fixed in ice-cold pre-fixative mix (4%
792 paraformaldehyde, 0.01% glutaraldehyde, 0.05% saponin, in CB) for 20 min at 4°C. Cells were
793 then incubated with ice-cold fixative mix (4% paraformaldehyde, 0.01% glutaraldehyde, in CB)
794 for 100 min at 4°C. Fixed cells were washed with CB twice and quenched by addition of 50
795 mmol/L NH_4Cl in CB for 5 min at RT. Protease digestion (1:2000 dilution) was performed for 10
796 min at RT using Protease-QS solution in PBS followed by 2 washes with 1X PBS. For RNA FISH,
797 QuantiGene ViewRNA ISH Cell Assay (Thermo Fisher Scientific) was used according to the
798 manufacturer's protocol. A custom-made probe for human pre-18S rRNA 5'ITS1 (internal
799 transcribed spacer 1) (5′-CCTCGCCCTCCGGGCTCCGTTAATGATC-3′) was used[44]. Cells were
800 washed four times with PBS-S (0.05% Saponin, in PBS) for 5 min at 20°C, counterstained with
801 DAPI for 10 min at RT, and then washed twice with 1X PBS. Images were acquired using a Zeiss
802 LSM-780 confocal microscope. Image analysis was performed using FIJI/ImageJ software
803 v1.53f51. Briefly, cell border and nuclear border were drawn and marked as region of interest

804 (ROI) and the number of particles (mRNA foci) within the ROI were calculated. The number of
805 cytoplasmic signals was calculated as the number of 5'ITS1 FISH signals within the cell border
806 subtracted by the number of signals within the nuclear boundary. The total number of 5'ITS1 FISH
807 signals per cell and the ratio of cytoplasmic to nuclear FISH signals per cell were plotted using
808 GraphPad Prism 10.2.0.
809
810 **Cell processing for phospho-proteomic analysis**
811 $2x10^6$ NIH 3T3 cells were seeded in 150mm plates and cultured for 24 h in DMEM media
812 containing 10% calf serum. The media was replaced by DMEM containing 0.1% calf serum for
813 24 h, after which the cells were stimulated with 15% calf serum and harvested at 0.5, 2, 4, 6 and 8
814 h. For harvesting, cells were washed twice with cold PBS, collected by scraping gently using a
815 Cell Lifter (Corning Incorporated, 3008) and centrifuging at 1200 rpm for 3 min. Cells were
816 harvested and used for phospho-proteomic analysis. Three independent replicate experiments were
817 performed. $1x10^6$ A549 cells were seeded in 100mm plates and transduced with lentiviruses
818 expressing control shRNA or three different TOLLIP shRNAs. Media was replaced the next day.
819 After 24 h, cells were trypsinized, transferred to a 150mm plate and selected using puromycin
820 (2.5µg/ml) for 2 days and harvested as described above. Three replicate experiments were
821 performed for each shRNA construct.
822
823 **Phospho-proteomic analysis by mass spectrometry**
824 Serum stimulated or unstimulated (0 h) NIH 3T3 cells were harvested (see above) and lysed in
825 500µl urea lysis buffer (8M Urea; 50mM Hepes pH 8.3), sonicated on ice 3 times at 1 min intervals
826 followed by centrifugation at 14,000 rpm for 10 min at 4°C. Supernatants were collected and

827 protein concentrations analyzed using BCA reagent (Bio-Rad). 250 mg protein was taken from
828 each sample and the total volume was adjusted to 150 ul with 50 mM Hepes pH 8.3. The samples
829 were then treated with 10mM DDT for 30 min at room temperature. Samples were alkylated using
830 20mM 2-Iodoacetamide for 30 min in the dark. 900µl cold acetone was added to each sample and
831 left overnight at -20°C to precipitate proteins. The samples were centrifuged at 14,000 rpm for 10
832 min at 4°C and the protein precipitates were collected and resuspended in 50mM Hepes (pH 8.3).
833 Next, the protein samples were treated with 6.5µg trypsin and incubated overnight at 37°C to
834 generate tryptic peptides. The peptide samples were then dried under vacuum and resuspended in
835 100µl of 50mM Hepes (pH 8.3). Tandem mass tag (TMT) isobaric labeling (ThermoFisher, CA)
836 was performed at 1:4 ratio by weight of sample for 1 h, and the reaction was quenched with 5%
837 hydroxylamine. Different mass tags were used for peptides obtained from the NIH 3T3 cells
838 harvested at each time point after serum stimulation; technical replicates received the same set of
839 mass tags. Replicate experiments were analyzed in separate runs. TMT-labeled samples from each
840 run were mixed, concentrated, dried under vacuum, and resuspended in 0.1% trifluoroacetic acid.
841 To remove any uncoupled TMT, peptide samples were passed through empty C18 columns
842 (ThermoFisher, CA). Eluted TMT labeled peptides were enriched for phosphopeptides by TiO_2
843 affinity purification (High Select TiO_2 kit; Thermo-Scientific, #A32993). The enriched
844 phosphopeptides bound to TiO_2 beads were eluted by high pH solvent and dried under vacuum.
845 The flow through peptides and the phosphopeptides obtained from the various wash steps were
846 collected separately, dried under vacuum, and resuspended in 0.1% TFA and further enriched for
847 phosphopeptides using Fe-Oxide affinity purification (High Select Fe-NTA; Thermo-Scientific,
848 #A32992). The phosphopeptides on the Fe-Oxide beads were then eluted by high pH solvents and
849 combined with the TiO_2 eluate collected earlier to obtain the maximum yield of phosphopeptides.

850 The enriched phosphopeptides were fractionated by high pH (8.5) reverse phase (RP) on a Waters
851 Acquity UPLC system coupled to a fluorescence detector (Waters, Milford, MA). The fractions
852 were consolidated into 12 pools based on the chromatographic intensity. The flow-through and
853 wash solutions of the Fe-oxide steps were collected, dried under vacuum, fractionated by high pH
854 (8.5) RP chromatography, and consolidated into 24 pools based on the chromatographic intensity.
855 The fraction pools were lyophilized and stored at -80°C until analysis by mass spectrometry.

856 For A549 cells, each TMT run contained four channels: an shCtrl sample and samples from
857 three different TOLLIP shRNAs. The experiment was performed in triplicate, generating three
858 replicates with four channels each. The replicate experiments were analyzed separately, resulting
859 in 12 different phosphopeptide intensity measurements. TMT labeling and phosphopeptide
860 enrichment were performed as described for NIH 3T3 cells. Different mass tags were used for the
861 different cell types, while technical replicates received the same mass tags. Phosphopeptides were
862 enriched using TiO_2 affinity purification and Fe-Oxide affinity purification, fractionated and the
863 resulting fraction pools were lyophilized and stored at -80°C.

864 *Mass spectrometry data acquisition and analysis.* Data acquisition of TMT labeled peptides
865 from NIH 3T3 cells was performed using Fusion Orbitrap (Thermo Scientific) and data for A549
866 cells were acquired using a Q-Exactive HF mass spectrometer (Thermo Scientific). The dried
867 samples were reconstituted in 0.1% TFA and separated using a second dimension low pH gradient
868 using a nanoflow liquid chromatography (Thermo Easy nLC 1000, Thermo Scientific) coupled to
869 a mass spectrometer at 300 nl/min. The MS/MS analysis of the peptides along with the quantitative
870 analysis of the TMT tags were performed at high resolution of 50,000 (Fusion)/45,000 (HF) in the
871 orbitrap analyzer. Acquired MS/MS spectra were searched against mouse (for NIH 3T3) or human
872 (for A549) Uniprot protein databases along with a contaminant protein database, using a

873 SEQUEST and percolator validator algorithms in the Proteome Discoverer 2.2 software (Thermo
874 Scientific, CA). The precursor ion tolerance was set at 10 ppm and the fragment ions tolerance
875 was set at 0.02 Da along with methionine oxidation included as dynamic modification and TMT6
876 plex (229.163Da) set as a static modification of lysine and the N-termini of the peptide. For
877 phospho-enriched peptides, phosphorylation of serine, threonine and tyrosine was set as a dynamic
878 modification. Trypsin was specified as the proteolytic enzyme, with up to 2 missed cleavage sites
879 allowed. A reverse decoy database search strategy was used to control for the false discovery rate
880 and peptide identifications were validated using the percolator algorithm. Phosphopeptides and
881 flow-through peptides from three independent experiments were analyzed. The affinity purified
882 peptides were used to determine the abundance of phosphopeptides (denoted p-peptides), while
883 the flow-through peptides were used to measure the protein abundance.
884
885 **Bioinformatic analysis of LC-MS data**
886 All analyses using the MTM LC/MS/MS p-peptide and protein intensities were performed using
887 either R (Version 4.3.1) or in-house programs. The twelve A549 samples (shCtrl, shTOLLIP.1,
888 shTOLLIP.2 and shTOLLIP.3 groups, each transduced in triplicate) were analyzed using the mass
889 tags described above. The first step was to consistently scale the intensities in these 12 channels
890 for the p-peptides and proteins. Due to the varying number of missing intensities across the
891 channels, a MAS5 scaling was found to produce the most consistent results. A p-peptide was
892 removed from consideration if it did not have an observed intensity for at least two of the three
893 technical replicates in each A549 group, if it did not represent a phosphorylated protein, or if the
894 peptide sequence matched more than one protein. In certain cases, multiple p-peptides contain the
895 same phosphorylated serine, threonine, or tyrosine residue. So that they were not treated

896 independently, the Accession number and global position within the protein was used to sum the
897 intensities at each phosphorylation site (p-site). The ratio of the p-site intensity to its corresponding
898 protein intensity within the same channel was then determined. A p-site was removed if the p-
899 site/protein ratio was not present in at least two of the three technical replicates for all cell cultures.
900 The p-site/protein ratios were averaged across the two or three technical replicates for each
901 group, followed by averaging the average ratios across the three TOLLIP knockdown groups. This
902 overall TOLLIP knockdown p-site/protein ratio was divided by the average p-site/protein ratio for
903 the shCtrl control samples to obtain a fold-change for each p-site. The log2-transform of these fold
904 changes was converted to a z-scale and the p-sites that were below -1.5 were selected.
905 The residues surrounding each p-site were examined to determine potential matches to CK2,
906 AKT or CDK phosphorylation motifs. A putative CK2-mediated p-site was identified if it passed
907 one of the following two rules[42,66,67], given that the p-site is at position *n*:
908 1. An aspartic or glutamic acid at either positions *n*+1 or *n*+3 or both, at least two
909 acidic residues between positions *n*-1 and *n*+5, no proline or basic residues at position *n*+1,
910 and no more than two basic residues between positions *n*-1 and *n*+5.
911 2. If there are no aspartic or glutamic acid at either positions *n*+1 or *n*+3, there must
912 be at least three acidic residues between positions n-1 and n+6, no proline or basic residue
913 at position *n*+1, and no more than two basic residues between positions *n*-1 and *n*+6.
914 A p-site was identified as a putative AKT target if an arginine was present at n-5 and n-3, and
915 if a hydrophobic residue (alanine, phenylalanine, isoleucine, leucine, methionine, threonine,
916 valine, or tryptophan) was present at n+1. Predicted CDK p-sites contained a proline at n+1 and a
917 lysine or arginine at n+3.

918 The NIH 3T3 MTM data was treated similarly. Each of the three technical replicates at each
919 time point was normalized using a MAS5 scaling. This was performed separately for the total
920 protein and p-peptide data. Using the Accession number and global position within the protein, the
921 p-peptide intensities were collapsed into p-site intensities. p-site/protein ratios were determined
922 for each technical replicate at each time point. A p-site was removed if there were less than two
923 replicates with valid p-site/protein ratios at any time point. The p-site/protein ratios were averaged
924 for each time point. The average p-site/protein ratios at 0 min, 30 min and 2 h were then averaged.
925 The average p-site/protein ratios at 4 or 6 h were then divided by the average of the average p-
926 site/protein ratios at the 0-2 h time points, to represent the fold-change at 4 or 6 h. The log2-
927 transformed fold-change across all p-sties was converted to a Z-score, and p-sites with a Z-score
928 above 1.5 were considered up-regulated. For each set of up-regulated p-sites, the predicted CK2,
929 AKT, and CDK p-sites were determined using the motif rules described above. Frequency
930 distribution tables were generated using GraphPad prism 10.2.0. Using a bin width of 0.02, the
931 number of values in each bin and the mean value per bin were plotted on the Y and X axes,
932 respectively. Bin range was determined based on the distribution of the log2 fold changes within
933 the selected phospho-proteomic data.

934 DAVID analysis[68] was carried out for functional annotation of p-site lists; classifications
935 based on Biological Processes (GOTERM_BP_DIRECT) were obtained and plotted. Ingenuity
936 Pathway Analysis (IPA) software[69] was used to perform "Phosphorylation Analysis" to generate
937 phosphorylation/signaling networks. Proteins corresponding to the p-sites were used as identifiers
938 and uploaded into the application. Networks generated by the IPA analysis are indicative of
939 potential signaling cascades.

940

941 **RNA-sequencing**

942 *Library preparation*. A total of 9 RNA samples (shCtrl, shTOLLIP.1 and shTOLLIP.2, each
943 transduced in triplicate into A549 cells) were processed for library preparation using the Illumina
944 Stranded Total RNA Prep and Ribo-Zero Plus. Prepared libraries were sequenced on an Illumina
945 NovaSeq Xplus 10B platform. Paired-end reads were generated, with a total of 419 to 886 million
946 reads per sample after filtering.

947 *Data preprocessing and alignment*. Raw sequencing data underwent initial quality control
948 using FastQC[70]. Adapters and low-quality reads were removed using Cutadapt[71]. Clean reads were
949 then aligned to the reference genome (hg38) using the STAR aligner[72]. In addition, the gene
950 expression quantification analysis was performed for all samples using STAR/RSEM[73].

951 *Differential expression analysis*. Differential expression analysis was performed using the
952 DESeq2 package in R[74]. Raw counts were normalized and a negative binomial model was applied
953 to identify genes with significantly altered expression between experimental conditions
954 (shTOLLIP.1 and shTOLLIP.2 versus shCtrl, independently). Only genes differentially expressed
955 in both conditions (shTOLLIP.1 versus shCtrl and shTOLLIP.2 versus shCtrl) were considered,
956 based on an adjusted p-value cutoff of 0.05 and a mean fold change threshold of 0.5.

957 *Gene set enrichment analysis (GSEA)*. GSEA was conducted using the ClusterProfiler[75]
958 package in R. Pre-ranked gene lists, generated from the differential expression analysis results,
959 were used as input for GSEA. Enrichment analysis was performed against gene sets obtained from
960 the org.Hs.eg.db package[76]. The statistical significance of enrichment scores was assessed through
961 permutation testing, and adjusted p-values were computed to account for multiple comparisons.
962 The significance threshold for enriched gene sets was set at 0.05. Specific pathways analysis was
963 conducted using the fgsea package[77].

964

965 **Statistical analysis**

966 Statistical analysis was performed using GraphPad Prism 10.2.0. Statistical significance for
967 quantitation of immunoprecipitation experiments, RNPI, animal experiments (tumor lesion counts,
968 tumor area, immunohistochemistry), colony formation assays, RNA-FISH and SA-βGal assays
969 was calculated using two-tailed unpaired Student's t test. P-values less than 0.05 were considered
970 significant. The log-rank (Mantel-Cox) test was used for Kaplan–Meier survival analyses. Two-
971 way ANOVA was used to analyze growth curves.

972

973 ## References

974 1. Prior, I. A., Hood, F. E. & Hartley, J. L. The Frequency of Ras Mutations in Cancer. *Cancer*
975 *Research* **80**, 2969-2974 (2020).
976 2. Baines, A. T., Xu, D. & Der, C. J. Inhibition of Ras for cancer treatment: the search
977 continues. *Future Med Chem* **3**, 1787-1808 (2011).
978 3. Konieczkowski, D. J., Johannessen, C. M. & Garraway, L. A. A Convergence-Based
979 Framework for Cancer Drug Resistance. *Cancer Cell* **33**, 801-815 (2018).
980 4. Schneider, G., Schmidt-Supprian, M., Rad, R. & Saur, D. Tissue-specific tumorigenesis:
981 context matters. *Nat Rev Cancer* **17**, 239-253 (2017).
982 5. Tape, C. J.*, et al.* Oncogenic KRAS Regulates Tumor Cell Signaling via Stromal
983 Reciprocation. *Cell* **165**, 1818 (2016).
984 6. Gober, M. K., Flight, R. M., Lambert, J., Moseley, H., Stromberg, A. & Black, E. P.
985 Deregulation of a Network of mRNA and miRNA Genes Reveals That CK2 and MEK
986 Inhibitors May Synergize to Induce Apoptosis KRAS-Active NSCLC. *Cancer Inform* **18**,
987 1176935119843507 (2019).
988 7. Wang, H.*, et al.* An integrative pharmacogenomics analysis identifies therapeutic targets in
989 KRAS-mutant lung cancer. *EBioMedicine* **49**, 106-117 (2019).
990 8. Papke, B. & Der, C. J. Drugging RAS: Know the enemy. *Science* **355**, 1158-1163 (2017).

991 9. Moore, A. R., Rosenberg, S. C., McCormick, F. & Malek, S. RAS-targeted therapies: is the
992 undruggable drugged? *Nat Rev Drug Discov* **19**, 533-552 (2020).
993 10. The Cancer Genome Atlas Research Network. Comprehensive molecular profiling of lung
994 adenocarcinoma. *Nature* **511**, 543-550 (2014).
995 11. Yip-Schneider, M. T., Lin, A., Barnard, D., Sweeney, C. J. & Marshall, M. S. Lack of
996 elevated MAP kinase (Erk) activity in pancreatic carcinomas despite oncogenic K-ras
997 expression. *Int J Oncol* **15**, 271-279 (1999).
998 12. Omerovic, J., Hammond, D. E., Clague, M. J. & Prior, I. A. Ras isoform abundance and
999 signalling in human cancer cell lines. *Oncogene* **27**, 2754-2762 (2008).
1000 13. Yeh, J. J.*, et al.* KRAS/BRAF mutation status and ERK1/2 activation as biomarkers for
1001 MEK1/2 inhibitor therapy in colorectal cancer. *Mol Cancer Ther* **8**, 834-843 (2009).
1002 14. Lim, K. H.*, et al.* Activation of RalA is critical for Ras-induced tumorigenesis of human
1003 cells. *Cancer Cell* **7**, 533-545 (2005).
1004 15. Mizumoto, Y.*, et al.* Activation of ERK1/2 occurs independently of KRAS or BRAF status in
1005 endometrial cancer and is associated with favorable prognosis. *Cancer Sci* **98**, 652-658
1006 (2007).
1007 16. Murphy, J. E., Padilla, B. E., Hasdemir, B., Cottrell, G. S. & Bunnett, N. W. Endosomes: a
1008 legitimate platform for the signaling train. *Proc Natl Acad Sci USA* **106**, 17615-17622
1009 (2009).
1010 17. Basu, S. K.*, et al.* Oncogenic RAS-Induced Perinuclear Signaling Complexes Requiring
1011 KSR1 Regulate Signal Transmission to Downstream Targets. *Cancer Research* **78**, 891-908
1012 (2018).
1013 18. Mellman, I. & Yarden, Y. Endocytosis and cancer. *Cold Spring Harb Perspect Biol* **5**,
1014 a016949 (2013).
1015 19. Sigismund, S., Confalonieri, S., Ciliberto, A., Polo, S., Scita, G. & Di Fiore, P. P.
1016 Endocytosis and signaling: cell logistics shape the eukaryotic cell plan. *Physiol Rev* **92**, 273-
1017 366 (2012).
1018 20. Jongsma, M. L.*, et al.* An ER-Associated Pathway Defines Endosomal Architecture for
1019 Controlled Cargo Transport. *Cell* **166**, 152-166 (2016).

1020 21. Stewart, S., Sundaram, M., Zhang, Y., Lee, J., Han, M. & Guan, K. L. Kinase suppressor of
1021 Ras forms a multiprotein signaling complex and modulates MEK localization. *Mol Cell Biol*
1022 **19**, 5523-5534 (1999).
1023 22. Roy, F., Laberge, G., Douziech, M., Ferland-McCollough, D. & Therrien, M. KSR is a
1024 scaffold required for activation of the ERK/MAPK module. *Genes Dev* **16**, 427-438 (2002).
1025 23. Ritt, D. A., Zhou, M., Conrads, T. P., Veenstra, T. D., Copeland, T. D. & Morrison, D. K.
1026 CK2 Is a component of the KSR1 scaffold complex that contributes to Raf kinase activation.
1027 *Curr Biol* **17**, 179-184 (2007).
1028 24. Shtutman, M.*, et al.* Function-based gene identification using enzymatically generated
1029 normalized shRNA library and massive parallel sequencing. *Proc Natl Acad Sci USA* **107**,
1030 7377-7382 (2010).
1031 25. Wolf, J.*, et al.* A mammosphere formation RNAi screen reveals that ATG4A promotes a
1032 breast cancer stem-like phenotype. *Breast Cancer Res* **15**, R109 (2013).
1033 26. Vizeacoumar, F. J.*, et al.* A negative genetic interaction map in isogenic cancer cell lines
1034 reveals cancer cell vulnerabilities. *Mol Syst Biol* **9**, 696 (2013).
1035 27. Frodyma, D., Neilsen, B., Costanzo-Garvey, D., Fisher, K. & Lewis, R. Coordinating ERK
1036 signaling via the molecular scaffold Kinase Suppressor of Ras. *F1000Res* **6**, 1621 (2017).
1037 28. Michaud, N. R.*, et al.* KSR stimulates Raf-1 activity in a kinase-independent manner. *Proc*
1038 *Natl Acad Sci U S A* **94**, 12792-12796 (1997).
1039 29. Jacobs, D., Glossip, D., Xing, H., Muslin, A. J. & Kornfeld, K. Multiple docking sites on
1040 substrate proteins form a modular system that mediates recognition by ERK MAP kinase.
1041 *Genes Dev* **13**, 163-175 (1999).
1042 30. Cacace, A. M.*, et al.* Identification of constitutive and ras-inducible phosphorylation sites of
1043 KSR: implications for 14-3-3 binding, mitogen-activated protein kinase binding, and KSR
1044 overexpression. *Mol Cell Biol* **19**, 229-240 (1999).
1045 31. McKay, M. M., Ritt, D. A. & Morrison, D. K. Signaling dynamics of the KSR1 scaffold
1046 complex. *Proc Natl Acad Sci USA* **106**, 11022-11027 (2009).
1047 32. Ciarrocchi, A.*, et al.* Tollip is a mediator of protein sumoylation. *PLoS One* **4**, e4404 (2009).
1048 33. Burns, K.*, et al.* Tollip, a new component of the IL-1RI pathway, links IRAK to the IL-1
1049 receptor. *Nat Cell Biol* **2**, 346-351 (2000).

1050 34. Shih, S. C., Prag, G., Francis, S. A., Sutanto, M. A., Hurley, J. H. & Hicke, L. A ubiquitin-
1051 binding motif required for intramolecular monoubiquitylation, the CUE domain. *EMBO J* **22**,
1052 1273-1281 (2003).
1053 35. Yamakami, M., Yoshimori, T. & Yokosawa, H. Tom1, a VHS domain-containing protein,
1054 interacts with tollip, ubiquitin, and clathrin. *J Biol Chem* **278**, 52865-52872 (2003).
1055 36. Jumper, J.*, et al.* Highly accurate protein structure prediction with AlphaFold. *Nature* **596**,
1056 583-589 (2021).
1057 37. Sun, Y., Cheng, Z. & Liu, S. MCM2 in human cancer: functions, mechanisms, and clinical
1058 significance. *Mol Med* **28**, 128 (2022).
1059 38. Tsuji, T., Ficarro, S. B. & Jiang, W. Essential role of phosphorylation of MCM2 by
1060 Cdc7/Dbf4 in the initiation of DNA replication in mammalian cells. *Mol Biol Cell* **17**, 4459-
1061 4472 (2006).
1062 39. Li, X., Goobie, G. C. & Zhang, Y. Toll-interacting protein impacts on inflammation,
1063 autophagy, and vacuole trafficking in human disease. *Journal of molecular medicine* **99**, 21-
1064 31 (2021).
1065 40. Begka, C.*, et al.* Toll-Interacting Protein Regulates Immune Cell Infiltration and Promotes
1066 Colitis-Associated Cancer. *iScience* **23**, 100891 (2020).
1067 41. Purzner, T.*, et al.* Developmental phosphoproteomics identifies the kinase CK2 as a driver of
1068 Hedgehog signaling and a therapeutic target in medulloblastoma. *Sci Signal* **11**, (2018).
1069 42. Meggio, F. & Pinna, L. A. One-thousand-and-one substrates of protein kinase CK2? *FASEB*
1070 *J* **17**, 349-368 (2003).
1071 43. Widmann, B.*, et al.* The kinase activity of human Rio1 is required for final steps of
1072 cytoplasmic maturation of 40S subunits. *Mol Biol Cell* **23**, 22-35 (2012).
1073 44. Turowski, T. W.*, et al.* Rio1 mediates ATP-dependent final maturation of 40S ribosomal
1074 subunits. *Nucleic Acids Res* **42**, 12189-12199 (2014).
1075 45. Plassart, L.*, et al.* The final step of 40S ribosomal subunit maturation is controlled by a dual
1076 key lock. *eLife* **10**, (2021).
1077 46. Ameismeier, M.*, et al.* Structural basis for the final steps of human 40S ribosome maturation.
1078 *Nature* **587**, 683-687 (2020).
1079 47. Luo, J.*, et al.* A genome-wide RNAi screen identifies multiple synthetic lethal interactions
1080 with the Ras oncogene. *Cell* **137**, 835-848 (2009).

1081 48. Weinberg, F., *et al.* The Atypical Kinase RIOK1 Promotes Tumor Growth and Invasive
1082 Behavior. *EBioMedicine* **20**, 79-97 (2017).
1083 49. Hong, X., *et al.* Targeting posttranslational modifications of RIOK1 inhibits the progression
1084 of colorectal and gastric cancers. *eLife* **7**, (2018).
1085 50. Kubinski, K. & Maslyk, M. The Link between Protein Kinase CK2 and Atypical Kinase
1086 Rio1. *Pharmaceuticals* **10**, (2017).
1087 51. Toruń, A., *et al.* Endocytic Adaptor Protein Tollip Inhibits Canonical Wnt Signaling. *PLoS*
1088 *One* **10**, e0130818 (2015).
1089 52. Zhu, L., *et al.* Tollip, an intracellular trafficking protein, is a novel modulator of the
1090 transforming growth factor-β signaling pathway. *J Biol Chem* **287**, 39653-39663 (2012).
1091 53. Didierlaurent, A., *et al.* Tollip regulates proinflammatory responses to interleukin-1 and
1092 lipopolysaccharide. *Mol Cell Biol* **26**, 735-742 (2006).
1093 54. Pokatayev, V., *et al.* Homeostatic regulation of STING protein at the resting state by
1094 stabilizer TOLLIP. *Nat Immunol* **21**, 158-167 (2020).
1095 55. Thapa, N., Chen, M., Horn, H. T., Choi, S., Wen, T. & Anderson, R. A. Phosphatidylinositol-
1096 3-OH kinase signalling is spatially organized at endosomal compartments by microtubule-
1097 associated protein 4. *Nat Cell Biol* **22**, 1357-1370 (2020).
1098 56. Pelletier, J., Thomas, G. & Volarevic, S. Ribosome biogenesis in cancer: new players and
1099 therapeutic avenues. *Nat Rev Cancer* **18**, 51-63 (2018).
1100 57. Azman, M. S., *et al.* An ERK1/2-driven RNA-binding switch in nucleolin drives ribosome
1101 biogenesis and pancreatic tumorigenesis downstream of RAS oncogene. *EMBO J* **42**,
1102 e110902 (2023).
1103 58. Feldser, D. M., *et al.* Stage-specific sensitivity to p53 restoration during lung cancer
1104 progression. *Nature* **468**, 572-575 (2010).
1105 59. Johnson, L., *et al.* Somatic activation of the K-ras oncogene causes early onset lung cancer in
1106 mice. *Nature* **410**, 1111-1116 (2001).
1107 60. Tuveson, D. A., *et al.* Endogenous oncogenic K-ras(G12D) stimulates proliferation and
1108 widespread neoplastic and developmental defects. *Cancer Cell* **5**, 375-387 (2004).
1109 61. Hingorani, S. R., *et al.* Trp53R172H and KrasG12D cooperate to promote chromosomal
1110 instability and widely metastatic pancreatic ductal adenocarcinoma in mice. *Cancer Cell* **7**,
1111 469-483 (2005).

1112 62. Therrien, M., Michaud, N. R., Rubin, G. M. & Morrison, D. K. KSR modulates signal
1113 propagation within the MAPK cascade. *Genes Dev* **10**, 2684-2695 (1996).
1114 63. Campeau, E.*, et al.* A versatile viral system for expression and depletion of proteins in
1115 mammalian cells. *PLoS One* **4**, e6529 (2009).
1116 64. Boothe, T.*, et al.* Inter-domain tagging implicates caveolin-1 in insulin receptor trafficking
1117 and Erk signaling bias in pancreatic beta-cells. *Mol Metab* **5**, 366-378 (2016).
1118 65. Schindelin, J.*, et al.* Fiji: an open-source platform for biological-image analysis. *Nat Methods*
1119 **9**, 676-682 (2012).
1120 66. St-Denis, N.*, et al.* Systematic investigation of hierarchical phosphorylation by protein kinase
1121 CK2. *J Proteomics* **118**, 49-62 (2015).
1122 67. Wang, C.*, et al.* Determination of CK2 specificity and substrates by proteome-derived
1123 peptide libraries. *Journal of proteome research* **12**, 3813-3821 (2013).
1124 68. Sherman, B. T.*, et al.* DAVID: a web server for functional enrichment analysis and
1125 functional annotation of gene lists (2021 update). *Nucleic Acids Res*, (2022).
1126 69. Kramer, A., Green, J., Pollard, J., Jr. & Tugendreich, S. Causal analysis approaches in
1127 Ingenuity Pathway Analysis. *Bioinformatics* **30**, 523-530 (2014).
1128 70. Babraham Bioinformatics. A quality control tool for high throughput sequence data.
1129 (ed^(eds). Babraham Institute (2023).
1130 71. Martin, M. Cutadapt removes adapter sequences from high-throughput sequencing reads. In:
1131 *EMBnet* (ed^(eds) (2011).
1132 72. Dobin, A.*, et al.* STAR: ultrafast universal RNA-seq aligner. *Bioinformatics* **29**, 15-21
1133 (2013).
1134 73. Li, B. & Dewey, C. N. RSEM: accurate transcript quantification from RNA-Seq data with or
1135 without a reference genome. *BMC Bioinformatics* **12**, 323 (2011).
1136 74. Love, M. I., Huber, W. & Anders, S. Moderated estimation of fold change and dispersion for
1137 RNA-seq data with DESeq2. *Genome Biol* **15**, 550 (2014).
1138 75. Wu, T.*, et al.* clusterProfiler 4.0: A universal enrichment tool for interpreting omics data.
1139 *Innovation (Camb)* **2**, 100141 (2021).
1140 76. Carlson, M. org.Hs.eg.db: Genome wide annotation for Human. (ed^(eds). Bioconductor
1141 (2022).

1142 77. Korotkevich, G., Sukhov, V., Budin, N., Shpak, B., Artyomov, M. N. & Sergushichev, A.
1143 Fast gene set enrichment analysis. *bioRxiv*, 060012 (2021).
1144

1145 ## Figure legends

1146 **Fig. 1 | TOLLIP interacts with KSR1 and co-localizes with KSR1 and CK2α on RAB11A+**
1147 **perinuclear endosomes in tumor cells. a** Co-immunoprecipitation assay showing association of
1148 Pyo-KSR1 with endogenous TOLLIP in 293T cells. Data are mean ± s.d.; n = 3 independent
1149 experiments. **b** Live cell images demonstrating perinuclear localization of GFP-tagged TOLLIP in
1150 A549 lung tumor cells and pan-cytoplasmic distribution in non-transformed bronchial epithelial
1151 cells (HBEC). Right: relative nuclear proximity index (RNPI) measures the average distance of
1152 fluorescent signals to the nuclear membrane, per cell, normalized to a uniform distribution (see
1153 Methods). Data are means for A549 and HBEC; n, number of cells analyzed. **c**
1154 Immunofluorescence staining (A549 cells) demonstrating co-localization of TOLLIP with KSR1,
1155 CK2α and RAB11A but not p-ERK. Right: co-localization of TOLLIP with the other proteins was
1156 quantified using Manders r and Pearson's R; n, number of cells analyzed. **d** TOLLIP-EGFP shows
1157 partial co-localization with KSR1-mCherry and nearly complete overlap with CK2α-mCherry and
1158 RAB11A-tagRFP in A549 cells. Bottom: co-localization of TOLLIP with KSR1, CK2α and
1159 RAB11A was quantified using Manders r and Pearson's R; n, number of cells analyzed. **e**
1160 Proximity ligation assays (PLA) confirm the spatial overlap of TOLLIP with KSR1, CK2α, and
1161 KSR1 but not p-ERK in A549 cells. Bottom: PLA signal quantification (foci per cell); n, number
1162 of cells analyzed. **f** Fluorescently-tagged KSR1, CK2α, TOLLIP and RAB11A are present on
1163 endosomal vesicles embedded within the ER network, labeled with Sec61β-GFP, in A549 cells.
1164 Statistical significance for co-immunoprecipitation assays and RNPI was calculated using two-
1165 tailed unpaired Student's t-test; *$P \leq 0.05$, ****$P \leq 0.0001$, ns not significant.
1166

1167 **Fig. 2 | TOLLIP is required for perinuclear localization of CK2α and KSR1 and**
1168 **proliferation/survival of tumor cells but is dispensable in normal cells. a** TOLLIP depletion in
1169 A549 cells causes pan-cytoplasmic dispersal of KSR1, CK2α and RAB11A. Right: RNPI analysis
1170 for each protein in control and TOLLIP knockdown cells; *n*, number of cells analyzed. **b** TOLLIP
1171 silencing reduces proliferation/survival of A549 and PANC1 tumor cells. Data are mean ± s.d.; *n*
1172 = 3 independent experiments. Insets: immunoblots verifying TOLLIP knockdown. **c** TOLLIP-
1173 depleted A549 cells display increased senescence (SA-βGal positivity) and apoptosis (cleaved
1174 CASPASE-3). SA-βGal data are mean ± s.d.; $n \geq 75$ cells analyzed per sample. **d** TOLLIP
1175 silencing does not affect proliferation of HBEC cells. Data are mean ± s.d.; $n = 3$ independent
1176 experiments. Inset shows immunoblots verifying TOLLIP depletion. **e**,**f** RAB11A depletion causes
1177 more uniform cytoplasmic distributions of TOLLIP (**e**), KSR1 and CK2α (**f**). A549 cells
1178 expressing RAB11A knockdown or control vectors were analyzed by IF staining for the indicated
1179 proteins. Right: RNPI analysis for each protein in control and RAB11A-depleted cells; *n*, number
1180 of cells analyzed.
1181 Two-way ANOVA was used to analyze growth curves. Statistical significance for SA-βGal assays
1182 and RNPI was determined using two-tailed unpaired Student's *t*-test; $^{*}P \leq 0.05$, $^{**}P \leq 0.01$, $^{***}P$
1183 ≤ 0.001, $^{****}P \leq 0.0001$.
1184
1185 **Fig. 3 | TOLLIP and KSR1 interact through conserved domains in each protein. a** Mapping
1186 the KSR1-interacting region of Tollip. HA-tagged full-length and mutant rat Tollip proteins were
1187 co-expressed with Pyo-KSR1 in HEK293T cells. Input lysates and Pyo IP samples were analyzed
1188 by immunoblotting for HA (see also Supplementary Fig. 3b) and binding intensity (IP/input) was
1189 determined and normalized to WT Tollip. Data are mean ± s.d.; $n = 3$ independent experiments.

1190 TBD, TOM1 binding domain; C2, lipid binding domain; CUE, ubiquitin binding domain. **b** A
1191 model of human TOLLIP predicted by AlphaFold2[36] depicts the KSR1 binding region forming a
1192 β-hairpin fold. Arrows point to the boundaries of the conserved 18 aa core sequence. *C. elegans*
1193 Tollip (bottom), which lacks the conserved KSR1 binding sequence, is not predicted to form the
1194 β-hairpin. **c** Subcellular localization of WT Tollip and selected deletion mutants fused to GFP.
1195 Proteins were expressed in A549 cells and imaged by fluorescence microscopy. Bottom: RNPI
1196 analysis for each protein; *n*, number of cells analyzed.
1197 Two-tailed unpaired Student's *t*-test was performed for IP quantification and RNPI data; $*P \leq$
1198 0.05, $****P \leq 0.0001$.
1199
1200 **Fig. 4 | *TOLLIP* is a dependency gene in *KRAS*- and *NRAS*-transformed cells. a** Control or
1201 Tollip-depleted NIH 3T3 cells were transduced with lentiviruses carrying $HRAS^{G12V}$, $KRAS^{G12V}$ or
1202 no insert (Ctrl) and immunostained for CK2α and KSR1. Immunoblots confirming Tollip
1203 knockdown are shown in Supplementary Fig. 4b,c. Bottom: RNPI analysis for CK2α and KSR1
1204 in each cell population; *n*, number of cells analyzed. **b** TOLLIP silencing does not affect
1205 proliferation of T24 cells (human urinary bladder carcinoma; $HRAS^{G12V}$). Data are mean ± s.d.; *n*
1206 = 3 independent experiments. Inset: immunoblot verifying TOLLIP depletion. **c** Perinuclear
1207 partitioning of KSR1 and CK2α in T24 cells is independent of TOLLIP. CK2α and KSR1
1208 localization in control and TOLLIP-depleted cells was analyzed by immunostaining. TOLLIP IF
1209 staining confirms silencing efficiency. Right: RNPI analysis of CK2α and KSR1; *n*, number of
1210 cells analyzed. **d** Clonogenic growth assays for a panel of human tumor cell lines carrying *KRAS*
1211 or *NRAS* mutations, comparing control and TOLLIP knockdown conditions. Data are mean ± s.d.,
1212 *n* = 3 independent experiments. A549 and H1299, non-small cell lung adenocarcinoma; PANC1

1213 and MIA PaCa-2, pancreatic ductal adenocarcinoma; MDA-MB-231, breast cancer; HepG2,
1214 hepatocarcinoma. Oncogenic mutations in each cell line are shown. Immunoblots confirm TOLLIP
1215 knockdown efficiency.
1216 Growth curves were analyzed by two-way ANOVA. RNPI and clonogenic growth assays were
1217 evaluated using two-tailed unpaired Student's *t*-test; $*P \leq 0.05$, $**P \leq 0.01$, $***P \leq 0.001$, $****P$
1218 ≤ 0.0001.
1219
1220 **Fig. 5 | Tollip is required for progression to adenocarcinoma in a *Kras^{G12D}*-driven model of**
1221 **lung tumorigenesis. a** Kaplan-Meier survival curves for *Tollip$^{+/+}$;LSL-Kras^{G12D}* and
1222 *Tollip$^{-/-}$;LSL-Kras^{G12D}* mice. Ad.Cre virus was delivered by intratracheal instillation in 10-week-
1223 old mice to initiate lung tumorigenesis. Virus administration corresponds to day 1 of the survival
1224 study. *Tollip$^{+/+}$*, $n = 18$; *Tollip$^{-/-}$*, $n = 19$. **b** Representative H&E images for lung hyperplasia and
1225 adenoma (benign) and ADC (malignant) lesions from *Tollip$^{+/+}$* animals. **c** Hyperplasia burdens in
1226 the two strains at clinical sacrifice, measured by HALO image analysis and plotted as % lung area.
1227 **d** Adenoma and ADC lesions/mouse, as determined by histopathological examination. **e** Most
1228 severe tumor grade observed in each genotype. Scoring is based on histopathological examination
1229 of lung lesions. **f** Immune infiltration in lung lesions, as determined by IHC staining for the pan-
1230 immune cell marker CD45 in adenomas and ADCs. Data represent % CD45 positive cells in each
1231 type of lesion, per animal. **g** Lung nodules in athymic *nu/nu* mice 11 weeks after tail vein injection
1232 of $1x10^6$ A549 cells. Cells were infected with a control lentivirus (shCtrl) or two different TOLLIP
1233 shRNA vectors prior to injection. TOLLIP knockdown cells produced a maximum of two lung
1234 nodules per animal. Left: immunoblots showing TOLLIP knockdown efficiency.

1235 The Mantel-Cox log-rank test was used to evaluate Kaplan–Meier survival data. Statistical
1236 significance for tumor burdens (**c**, **d**, **f**, **g**) was calculated using two-tailed unpaired Student's *t*-
1237 test. Fisher's exact test was used to compare the most severe lesion data (**e**). *$P \leq 0.05$, ****$P \leq$
1238 0.0001.
1239
1240 **Fig. 6 | Changes in phosphoproteomes upon TOLLIP depletion in A549 cells or coinciding**
1241 **with PSC formation in GF-stimulated cells. a** Phosphoproteome analysis pipeline for A549 cells
1242 without and with TOLLIP depletion. **b** Ranked gene ontology categories (GO, biological process)
1243 for proteins corresponding to p-sites down-regulated in TOLLIP-depleted cells ($Z \leq -1.5$). **c**
1244 Sequences of predicted CK2 motifs corresponding to down-regulated p-sites. Right: heat maps
1245 showing Z-scores and $\log_2$ fold changes for each p-site. **d** GO analysis of proteins corresponding
1246 to TOLLIP-dependent CK2 p-sites listed in **c**. **e** Phosphoproteome analysis pipeline for serum-
1247 stimulated NIH 3T3 cells. KSR1 and CK2α form PSCs at 4 and 6 h, while p-ERK becomes
1248 perinuclear at 6 h[17]. **f** Frequency of CK2 motifs in p-sites that increase at 4 and 6 h in NIH 3T3
1249 cells ($Z \geq 1.5$) compared to all p-sites. **g** List of common CK2 p-sites up-regulated at both 4 and 6
1250 h. **h** Ranked GO categories (biological process) for common CK2 p-sites shown in **g**.
1251 Statistical significance of CK2 site enrichment in NIH 3T3 4 h $Z < -1.5$ p-sites relative to all p-sites
1252 (**f**) was assessed using the one-tailed Binomial test.
1253
1254 **Fig. 7 | TOLLIP-dependent phosphorylation on RIOK1 Ser22, a CK2 site, stimulates its pro-**
1255 **oncogenic function in tumor cells. a** RIOK1 Ser22 (arrow) and flanking sequences are conserved
1256 in mammals and absent in other species homologs, including other vertebrates. Acidic residues
1257 contributing to the CK2 motif are highlighted. **b** RIOK1 Ser22 phosphorylation is augmented by

1258 co-expression of $KRAS^{G12V}$. Flagged-tagged RIOK1 WT and S22A constructs were expressed in
1259 HEK293T cells, ± $KRAS^{G12V}$. Lysates were analyzed by immunoblotting using a pSer22 RIOK1
1260 antibody. pSer22 RIOK1 levels normalized to total RIOK1 are shown on the right. Data are mean
1261 ± s.d.; n = 3 independent experiments. **c** TOLLIP depletion decreases RIOK1 Ser22
1262 phosphorylation in A549 cells. RIOK1 pSer22 levels normalized to total RIOK1 are shown on the
1263 right. Data are mean ± s.d.; n = 3 independent experiments. **d** RIOK1 Ser22 phosphorylation in
1264 *HRAS* mutant T24 cells is unaffected by TOLLIP knockdown. pSer22 RIOK1 levels normalized
1265 to total RIOK1 are shown on the right. Data are mean ± s.d.; n = 3 independent experiments. **e**
1266 Ser22 is required for RIOK1 function in A549 cells. RIOK1 was depleted in A549 cells using two
1267 different inducible shRIOK1 constructs targeting the 3'UTR. *WT* and S22A and S22D mutant
1268 constructs lacking the 3'UTR were expressed in RIOK1-silenced cells to assess their ability to
1269 rescue clonogenic growth. Immunoblot shows depletion of endogenous RIOK1 (E) and levels of
1270 over-expressed FLAG-RIOK1 proteins (OE). Colony data are mean ± s.d.; n = 3 independent
1271 experiments. **f** TOLLIP and RIOK1 are required for efficient 18S rRNA processing. A549 cells
1272 were depleted for RIOK1 or TOLLIP and analyzed by RNA FISH using a 5'ITS probe to detect
1273 the unprocessed 18S precursor. Insets depict enlarged areas encompassing the nucleus. Total
1274 number of FISH signals and the cytoplasmic/nuclear ratio per cell were quantified (lower panel);
1275 n, number of cells analyzed.
1276 Two-tailed unpaired Student's t-test was used to analyze pSer22 RIOK1 levels and 5'ITS1 RNA
1277 FISH data; $^{*}P \leq 0.05$, $^{***}P \leq 0.001$, $^{****}P \leq 0.0001$.

Figure 1

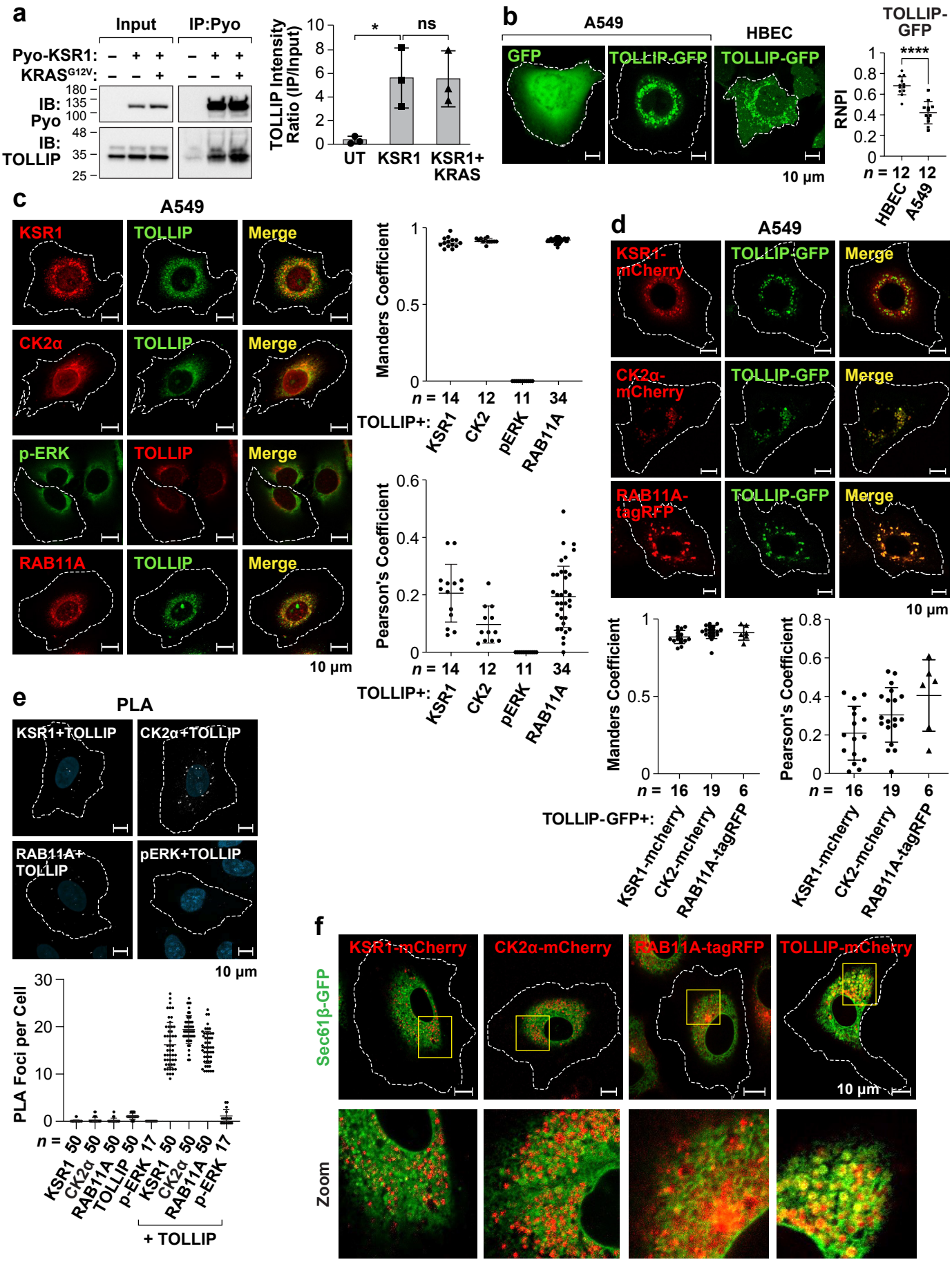
a
Input
IP:Pyo
Pyo-KSR1:
KRAS^{G12V}:
IB: Pyo
IB: TOLLIP
180
135
100
48
35
25
TOLLIP Intensity Ratio (IP/Input)
*
ns
UT
KSR1
KSR1+ KRAS
b
A549
HBEC
GFP
TOLLIP-GFP
10 µm
RNPI
****
n = 12 12
HBEC
A549
c
A549
KSR1
TOLLIP
Merge
CK2α
p-ERK
RAB11A
Manders Coefficient
Pearson's Coefficient
n = 14 12 11 34
TOLLIP+:
KSR1
CK2
pERK
RAB11A
d
A549
KSR1-mCherry
CK2α-mCherry
RAB11A-tagRFP
TOLLIP-GFP
n = 16 19 6
TOLLIP-GFP+:
KSR1-mcherry
CK2-mcherry
RAB11A-tagRFP
e
PLA
KSR1+TOLLIP
CK2α+TOLLIP
RAB11A+ TOLLIP
pERK+TOLLIP
PLA Foci per Cell
n = 50 50 50 50 17 50 50 50 17
+ TOLLIP
f
KSR1-mCherry
CK2α-mCherry
RAB11A-tagRFP
TOLLIP-mCherry
Sec61β-GFP
Zoom

Figure 2

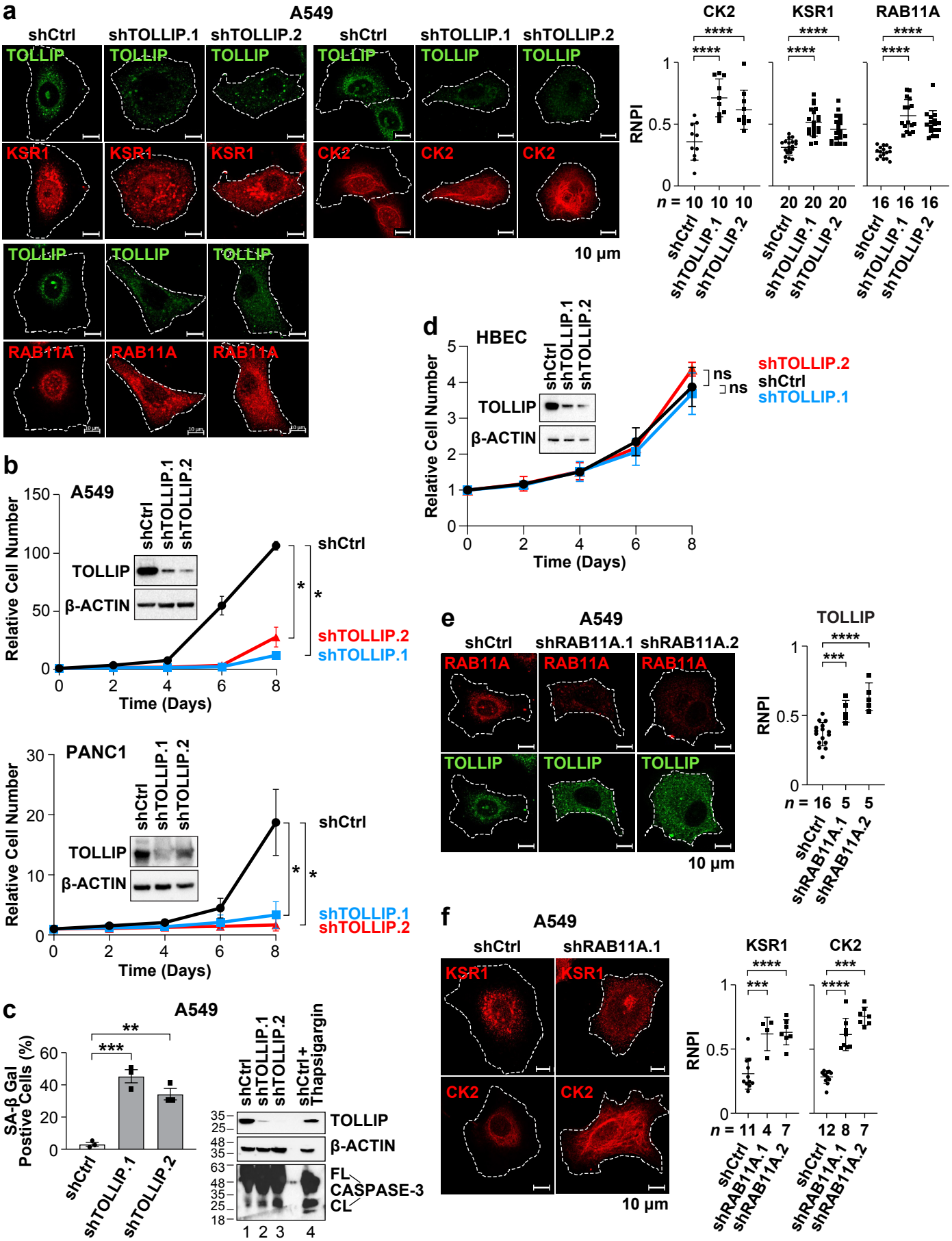
a
A549
shCtrl
shTOLLIP.1
shTOLLIP.2
TOLLIP
KSR1
CK2
RAB11A
10 µm
RNPI
n = 10 10 10
20 20 20
16 16 16
b
A549
Relative Cell Number
Time (Days)
TOLLIP
β-ACTIN
shCtrl
shTOLLIP.2
shTOLLIP.1
PANC1
c
A549
SA-β Gal Postive Cells (%)
shCtrl + Thapsigargin
FL
CASPASE-3
CL
d
HBEC
ns
e
shRAB11A.1
shRAB11A.2
n = 16 5 5
f
n = 11 4 7
12 8 7

Figure 3

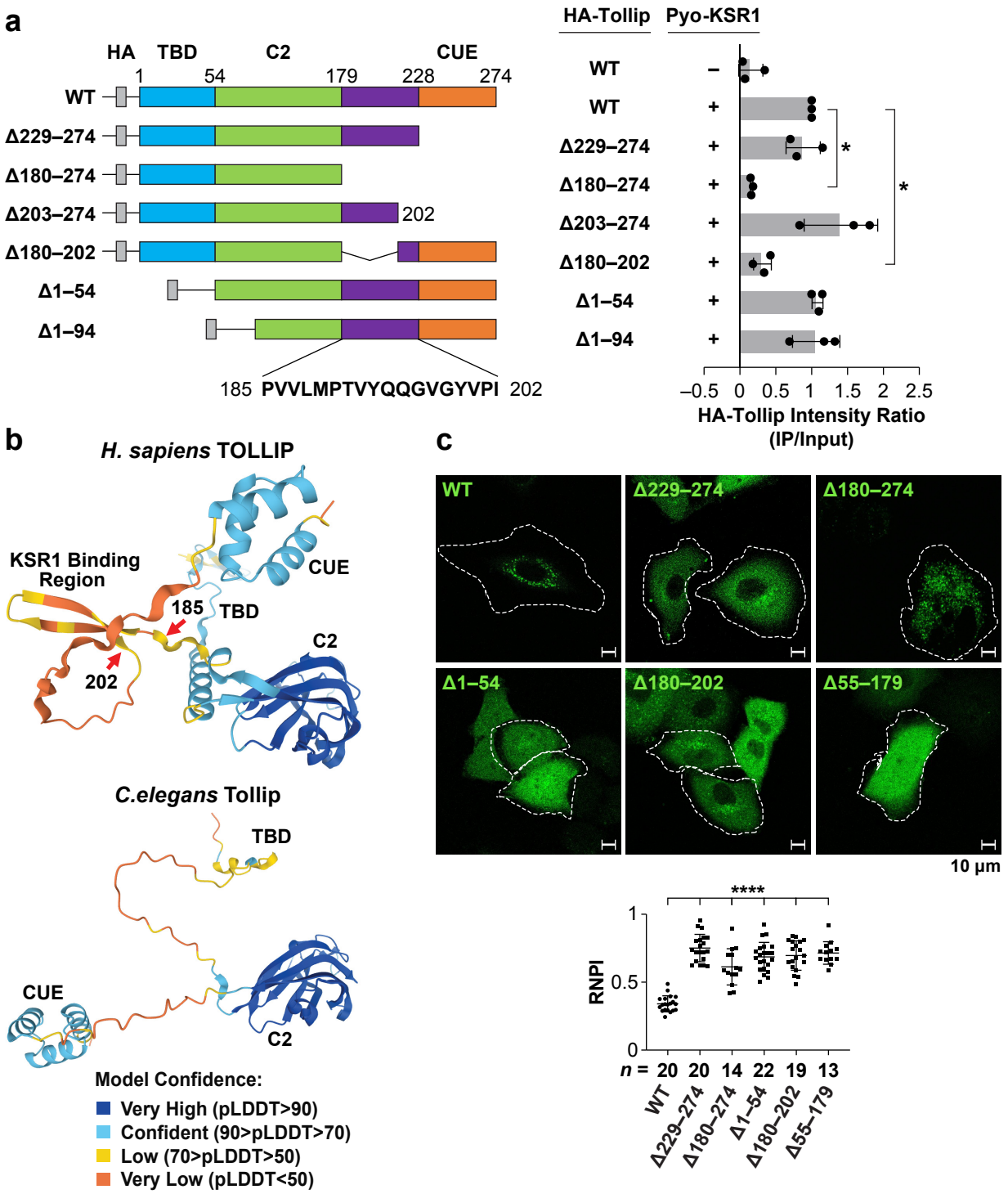
a
HA
TBD
C2
CUE
1
54
179
228
274
WT
Δ229–274
Δ180–274
Δ203–274
202
Δ180–202
Δ1–54
Δ1–94
185 PVVLMPTVYQQGVGYVPI 202
HA-Tollip
Pyo-KSR1
WT
WT
Δ229–274
Δ180–274
Δ203–274
Δ180–202
Δ1–54
Δ1–94
–0.5 0 0.5 1 1.5 2 2.5
HA-Tollip Intensity Ratio
(IP/Input)
b
H. sapiens TOLLIP
KSR1 Binding Region
CUE
185
TBD
C2
202
C.elegans Tollip
TBD
CUE
C2
Model Confidence:
Very High (pLDDT>90)
Confident (90>pLDDT>70)
Low (70>pLDDT>50)
Very Low (pLDDT<50)
c
WT
Δ229–274
Δ180–274
Δ1–54
Δ180–202
Δ55–179
10 µm
****
RNPI
n = 20 20 14 22 19 13
WT
Δ229–274
Δ180–274
Δ1–54
Δ180–202
Δ55–179

Figure 4

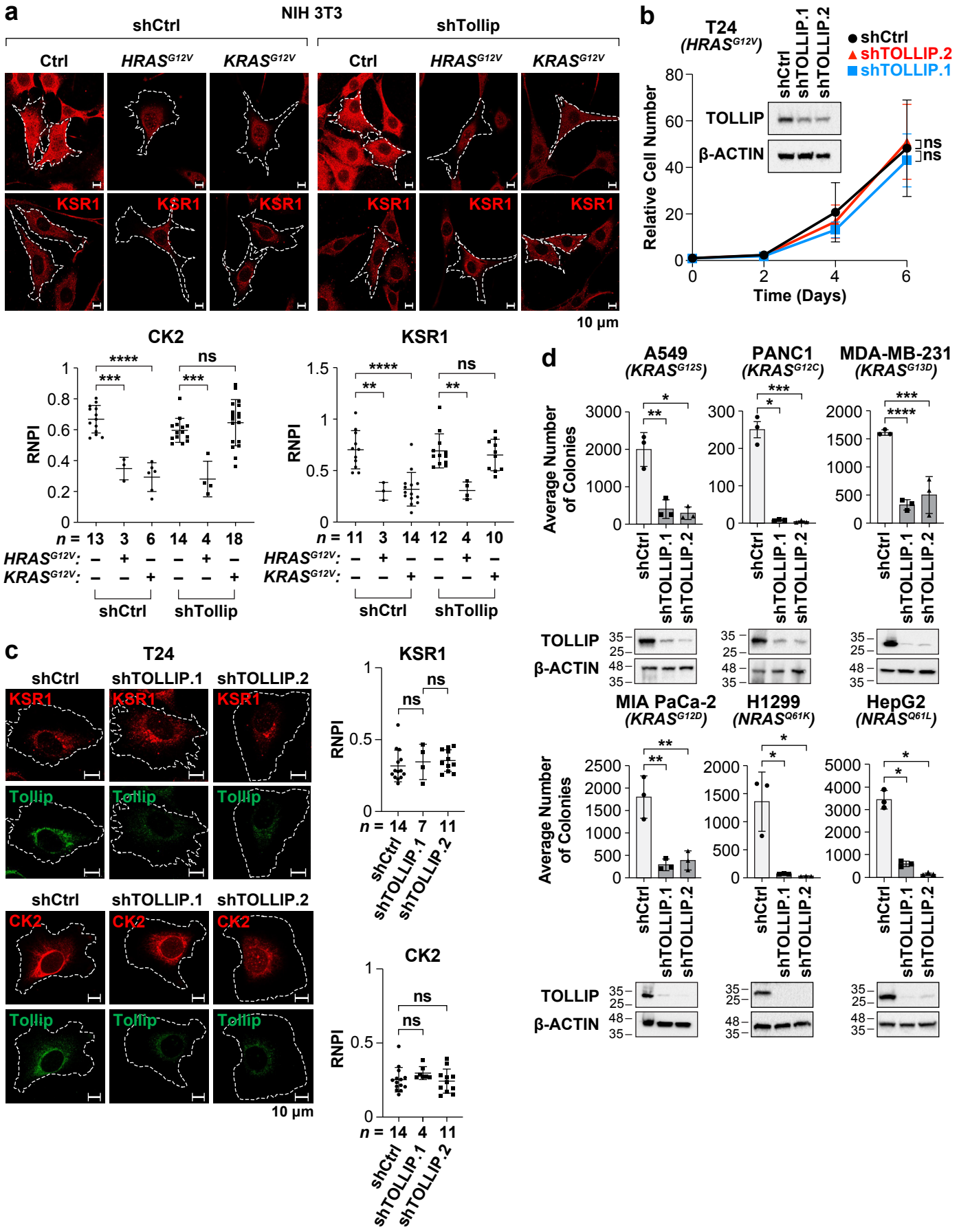
a
NIH 3T3
shCtrl
shTollip
Ctrl
HRASG12V
KRASG12V
KSR1
10 µm
CK2
KSR1
RNPI
n = 13 3 6 14 4 18
n = 11 3 14 12 4 10
HRASG12V:
KRASG12V:
shCtrl
shTollip
b
T24
(HRASG12V)
shCtrl
shTOLLIP.1
shTOLLIP.2
TOLLIP
β-ACTIN
Relative Cell Number
Time (Days)
ns
c
T24
Tollip
CK2
n = 14 7 11
n = 14 4 11
d
A549
(KRASG12S)
PANC1
(KRASG12C)
MDA-MB-231
(KRASG13D)
MIA PaCa-2
(KRASG12D)
H1299
(NRASQ61K)
HepG2
(NRASQ61L)
Average Number of Colonies

Figure 5

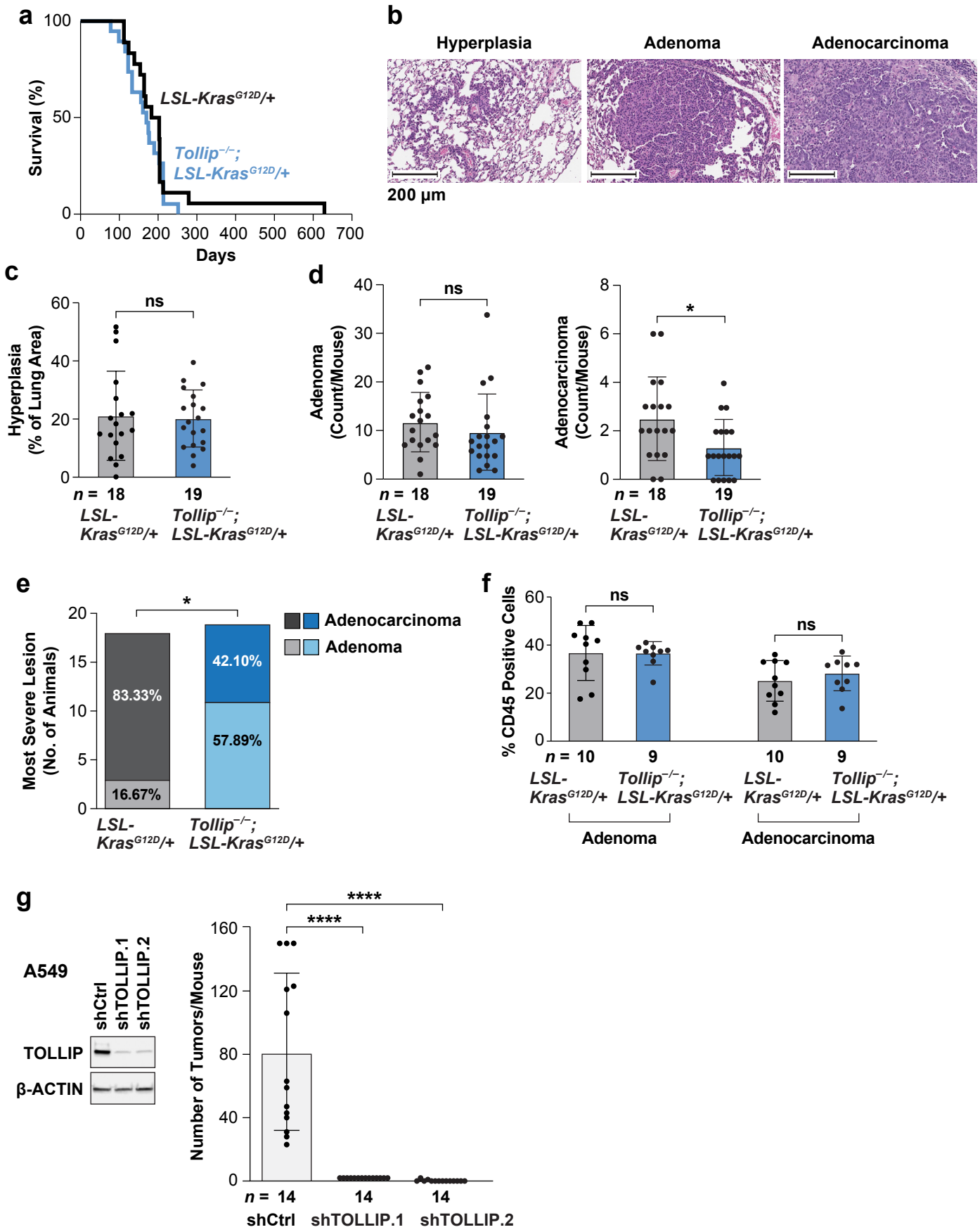
a
Survival (%)
Days
LSL-KrasG12D/+
Tollip−/−; LSL-KrasG12D/+
b
Hyperplasia
Adenoma
Adenocarcinoma
200 µm
c
Hyperplasia (% of Lung Area)
ns
n = 18
19
LSL-KrasG12D/+
Tollip−/−; LSL-KrasG12D/+
d
Adenoma (Count/Mouse)
ns
Adenocarcinoma (Count/Mouse)
*
e
Most Severe Lesion (No. of Animals)
*
Adenocarcinoma
Adenoma
83.33%
16.67%
42.10%
57.89%
f
% CD45 Positive Cells
ns
ns
Adenoma
Adenocarcinoma
g
A549
shCtrl
shTOLLIP.1
shTOLLIP.2
TOLLIP
β-ACTIN
Number of Tumors/Mouse
****
****

Figure 6

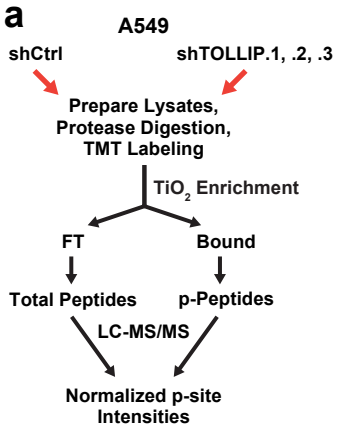

c

Name	Annotated Sequence
LSR	GWRARRPRARS493VDALDDLTPP
TRIP12	YGRVREDDEDS1317DDDGSDEEID
TRIP12	EDDEDSDDDGS1322DEEIDESLAA
TPD52L2	GDMRNSATFKS166FEDRVGTIKS
PDCD4	NSSRDSGRGDS76VSDSGSDALR
KRT18	MRNLKASLENS323LREVEARYAL
SH3KBP1	MFPSNFIKELS156GESDELGISQ
MCM2	GRMRRGLLYDS139DEEDEERPAR

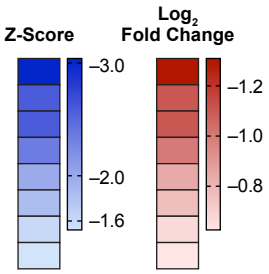

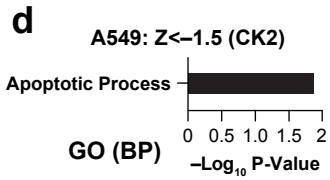

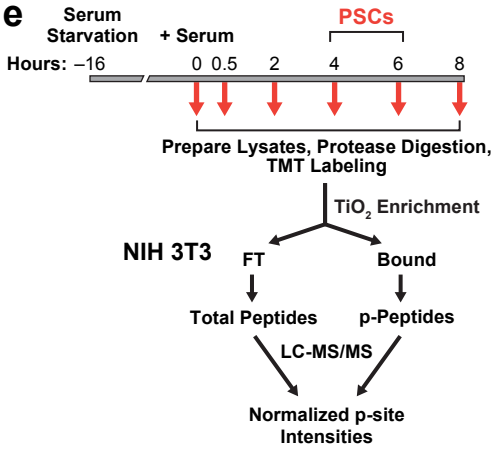

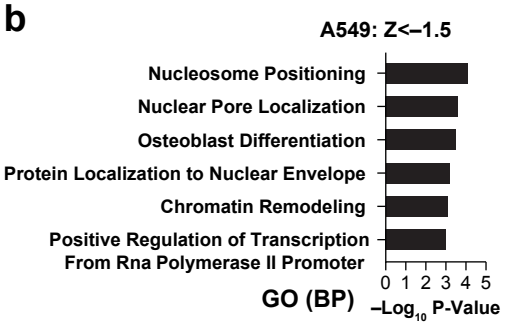

f

NIH 3T3

Set	p-sites	CK2 Sites	% CK2	P-Value (CK2)
All	3758	1279	34.03	
4h/(0-2h): Z>1.5	190	77	40.52	0.036
6h/(0-2h): Z>1.5	146	53	36.30	0.309

g

NIH 3T3: 4+6h Intersection (CK2 p-sites)

Name	Annotated Sequence
MYBBP1A	QLQHGEDEDS722DNEDNK
Pum1	KGGFGPRDADS247DENDKGEKKN
LRRC47	QHRES315GEGEEEVADSAR
Arnt	MCNDKERFARS77DDEQSSADKE
Nr2f6	DDSASPPGATS41DAEPGDEERP
Ppp1r11	YEKPRAFGESS79TESDEDEEEG
Polr3c	LIGKGKRRRSS205DEDATGEPKA
Pbdc1	KEEAAEKGADS184GGEKEEGANR
PRRC2B	IASETHSEGS1154EYEELPK
Anp32b	EAPDSDVEVDS164VEEAPDSDGE
Anp32b	EVDSVEEAPDS171DGEVDGVDKE
Cdc42ep4	TSKAREADDES64LDEQASASKL
PTPN21	SLSDATMLIHS710SEEDEDLEEDSSR
PTPN21	SLSDATMLIHSS711EEDEDLEEDSSR
Map1b	LSPMDEPVPDS1382ESPVEKVLSP
MCM6	EIESEIDS762EEELINK
Sipa1l2	SPRRSLYRTLS1488DESVCSNRRG
Iws1	DSDGENKREDS289EVQNESDGHT
Gys1	SLSRHSSPHQS657EDEEEPRDGP
USP34	RESTGSYS1520DLYPDSDDSSEDQVENSK
USP34	RESTGSYSDLYPDS1526DDSSEDQVENSK
CTR9	IADEGHPRNS1037NSDSDDDERPNR
CTR9	IADEGHPRNSNS1039DSDDDERPNR
CTR9	IADEGHPRNSNSDS1041DDDERPNR

h

NIH 3T3: 4+6h Intersection
Z<–1.5 (CK2 p-sites)

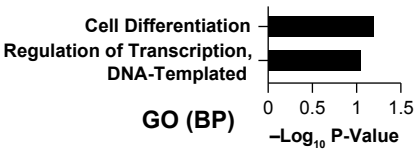

Figure 7

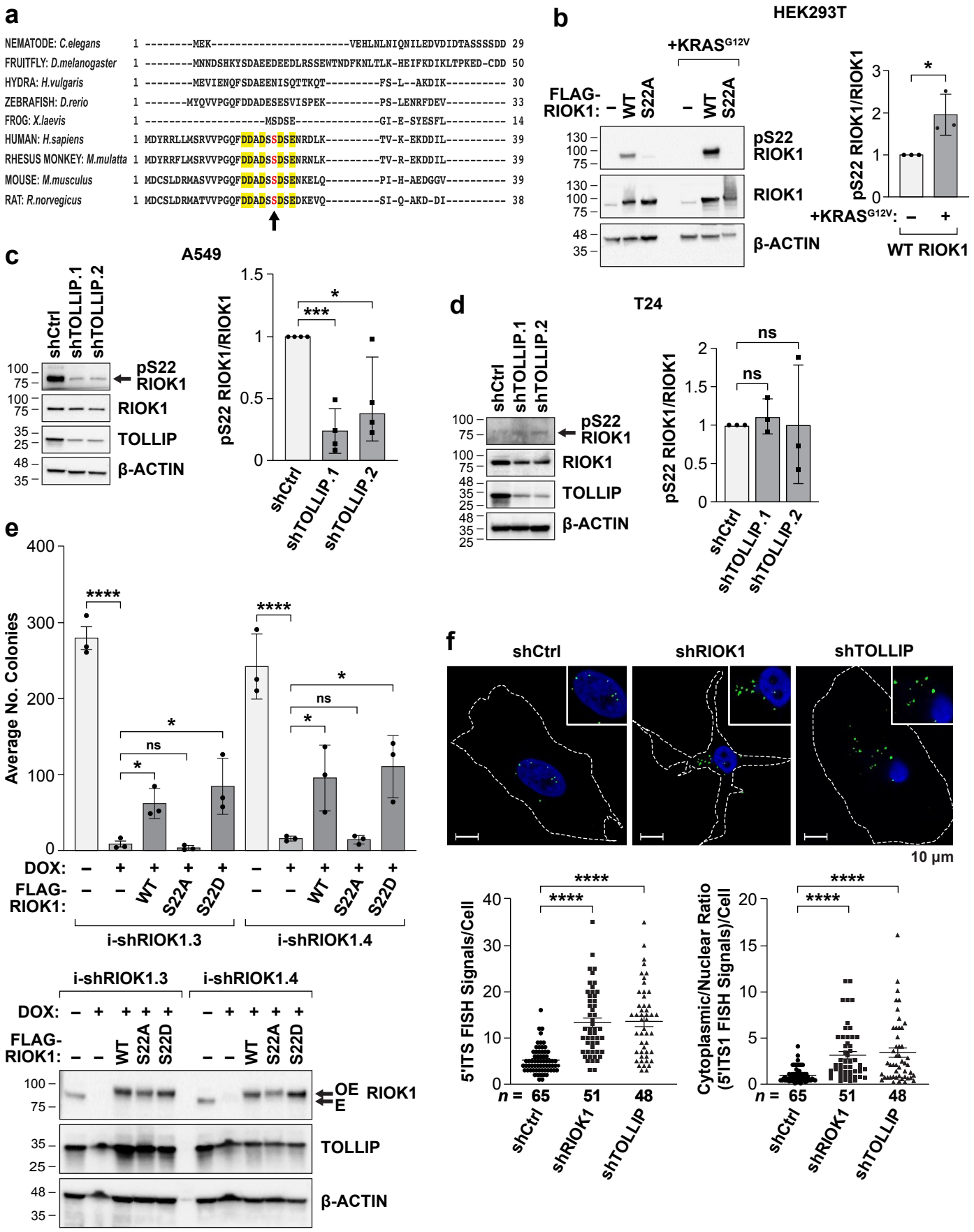
a
NEMATODE: C.elegans 1 --------MEK----------VEHLNLNIQNILEDVDIDTASSSSDD 29
FRUITFLY: D.melanogaster 1 --------MNNDSHKYSDAEEDEEDLRSSEWTNDFKNLTLK-HEIFKDIKLTPKED-CDD 50
HYDRA: H.vulgaris 1 --------MEVIENQFSDAEENISQTTKQT---------FS-L--AKDIK---------- 30
ZEBRAFISH: D.rerio 1 -------MYQVVPGQFDDADESESVISPEK---------PS-LENRFDEV---------- 33
FROG: X.laevis 1 ----------MSDSE----------GI-E-SYESFL---------- 14
HUMAN: H.sapiens 1 MDYRRLLMSRVVPGQFDDADSSDSENRDLK---------TV-K-EKDDIL---------- 39
RHESUS MONKEY: M.mulatta 1 MDYRRFLMSRVVPGQFDDADSSDSENRNLK---------TV-R-EKDDIL---------- 39
MOUSE: M.musculus 1 MDCSLDRMASVVPGQFDDADSSDSENKELQ---------PI-H-AEDGGV---------- 39
RAT: R.norvegicus 1 MDCSLDRMATVVPGQFDDADSSDSEDKEVQ---------SI-Q-AKD-DI---------- 38
b
HEK293T
+KRAS G12V
FLAG-RIOK1: – WT S22A – WT S22A
pS22 RIOK1
RIOK1
β-ACTIN
pS22 RIOK1/RIOK1
+KRAS G12V: – +
WT RIOK1
c
A549
shCtrl shTOLLIP.1 shTOLLIP.2
pS22 RIOK1
RIOK1
TOLLIP
β-ACTIN
pS22 RIOK1/RIOK1
d
T24
shCtrl shTOLLIP.1 shTOLLIP.2
pS22 RIOK1
RIOK1
TOLLIP
β-ACTIN
pS22 RIOK1/RIOK1
ns
e
Average No. Colonies
DOX: – + + + + – + + + +
FLAG-RIOK1: – – WT S22A S22D – – WT S22A S22D
i-shRIOK1.3
i-shRIOK1.4
OE
E
RIOK1
TOLLIP
β-ACTIN
f
shCtrl
shRIOK1
shTOLLIP
10 µm
5'ITS FISH Signals/Cell
Cytoplasmic/Nuclear Ratio (5'ITS1 FISH Signals)/Cell
n = 65 51 48